Trinity College Dublin
Coláiste na Tríonóide, Baile Átha Cliath
The University of Dublin

School of Engineering
Department of Mechanical & Manufacturing Engineering

Dynamic Characterisation of the Sleeved Pneumatic Artificial Muscle

Tyron Pretorius

12308327

4th April 2017

A dissertation submitted in partial fulfilment of the degree of

MAI (Mechanical and Manufacturing Engineering)

Declaration

I have read and I understand the plagiarism provisions in the General Regulations of the University Calendar for the current year, found at **http://www.tcd.ie/calendar**.

I have also completed the Online Tutorial on avoiding plagiarism 'Ready Steady Write', located at **http://tcd-ie.libguides.com/plagiarism/ready-steady-write**.

Pretorius

Abstract

Pneumatic Artificial Muscles (PAMs) are a compelling Biorobotic actuator, featuring high power to weight ratios and an innate compliance, ideal for lightweight, intrinsically safe actuated systems.

Performance limitations such as a short actuation range, low bandwidth, and poor positional accuracy reduce its practical applications. Furthermore, the merit of PAMs as biomimetic actuators is hindered by the necessity of ancillary valves and sensors, which add additional mass to a system while increasing volume and power requirements.

The focus of this thesis is thus on how the Sleeved Pneumatic Artificial Muscle (SPAM) can resolve the performance limitations associated with a traditional PAM. The SPAM has already been shown to significantly improve performance in the areas of contractile range, force output, air consumption, and pressure requirements.

The main objective of this research is to investigate and quantify the expected increase in response time of the SPAM in isometric, isotonic, and antagonistic operation. The dynamic testing of both the sleeved and non-sleeved McKibben muscles reveals the far superior performance attributes of the SPAM. The isometric (constant length) response time of the SPAM is at least 24% higher than the non-sleeved muscle for any contraction ratio (0-25%) and supply pressure (0-60psi) combination. Similarly, the isotonic (constant force) response of the SPAM is more than 25% faster through the same supply pressure range for an applied load of 20-180N.

The enhanced isometric and isotonic response of the SPAM in combination with its greater contractile range and force output translated to an antagonistic performance that far exceed that of the conventional muscle. The SPAM is able to move through much larger angular displacements and do so faster than the non-sleeved muscle even while lifting 3.5 times more weight. Finally, the SPAM is shown to have substantially greater resilience to disturbances (5^0,10^0, and 15^0 initial displacements), with settling times up to 10 less than the normal muscle.

The impact of ancillary hardware is also investigated by incorporating a pressure sensor inside the SPAM. Comparison of the pressure readings obtained on the inside of the SPAM and on the supply line to the SPAM revealed that there is no significant difference in the pressure at these two locations. However, the incorporation of the pressure sensor into the sleeved design does produce a more compact actuation system

Acknowledgements

I would first of all like to thank my supervisor Conor McGinn for all his gentle words of support and encouragement throughout the year. To the rest of the lads Eamo "Sesh Gremlin" Bourke, Paddy "Fifty Shades" Lynch, Cian "Always Swipe Right" Donovan , and Robbie "Wee Arse Nugget" Fryers (who actually didn't help out on the project but his "Nordy" banter warrants his inclusion on this esteemed list) I extend a big thanks not only for the help on the project but for the companionship and amusement throughout the year.

Last but not least, the greatest thanks of all goes to Micheal "Collins" Cullinan because without his constant help and direction over the course of the year, the title of this thesis would have been more along the lines of "An antagonistic muscle rig for paper weight applications".

Contents

Figures

1 Introduction

“Robotics is about us. It is the discipline of emulating our lives, of wondering how we work.” Rod Grupen, Co-Editor-in-Chief of the Robotics and Autonomous Systems Journal [1].

The latest development in Robotics has seen an increase in demand outside the long established niche of industrial automation. Inventions such as Google’s autonomous car [2], robotic vacuum cleaners [3], and Boston Dynamic’s emergency response robot; Atlas[4], are bringing robots to the forefront of our everyday lives. The ubiquity of increasingly autonomous robots has led to an increased emphasis on Human Robot Interaction (HRI).

The natural process of evolution has seen to the optimal development of human and animal morphologies to ensure survival in changing surroundings. Accordingly, it is logical that in order for robotic designs to thrive in the same environments they must follow the anatomy of these tailor made morphologies. The ergonomics of living spaces and their constituent elements has been catered to the size and shape of the human body, thereby giving humanoid robots an inherent advantage in effectively operating in and interacting with these environments. Similarly, the actuation method of a humanoid robot should be akin to that of human muscle and there is no better replica than the McKibben artificial muscle [5].

The McKibben muscle is a variant of a brand of actuator called the “Pneumatic Artificial Muscle” and features a number of characteristics that make it ideal for Human Robot Interaction (Table 1), none more so than its inherent compliance.

Advantages	Disadvantages
Adjustable Compliance [6,7]	Difficult to Model and Control [8–10]
Similarity to Human Muscle [10–12]	Temperature Dependent Materials [13–16]
High Power to Weight Ratios [11,17]	Low fatigue life [5,18]
Lightweight power source [6]	Friction induced hysteresis [9,16,19]
Quick Recharge Times [6]	Complex Fluid Dynamics [10,11,20–22]
Passive static stability [9,17]	Low Contraction Ratio [6,17]
Direct Mechanical Connection [6,23]	Ancillary Hardware Limitations [10,11]

Table 1 Advantages and disadvantages of PAMs

However, the cost of having a compliant actuator is that it is difficult to model and control [8–10]. Furthermore, although the materials used to construct the muscle are lightweight [6], they are heavily temperature dependent [13–16], have a low fatigue life [5,18], and they introduce a non-linear frictional behaviour into the system [9,16,19]. The aforementioned problems are no longer of serious concern due to the extensive research undertaken in these areas. Therefore, the biggest remaining obstacle to widespread implementation of PAMs is poor performance arising from its intrinsic design and peripheral hardware limitations.

The inability to exert a reasonable output force throughout the entirety of an already limited contractile range is an intrinsic flaw of PAMs, whereas the finite switching times and small orifice diameters of supporting valves provide an external constraint to system bandwidth and response time. Furthermore the mass, volume, and power requirements of these ancillary valves and sensors threaten the merit of the McKibben muscle as a biomimetic actuator.

Consequently, the overall goal of this research project is to analyse and address the physical limitations of the McKibben muscle to improve its suitability for Human Robot Interaction.

1.1 Objectives

1. Determination of the dynamic performance of a single SPAM

Isometric tests will be carried out on a single SPAM to determine the pressure step response over a supply pressure range of 10-60psi at 0-25% contraction. The time taken for the muscle to contract by a certain amount will also be investigated as a function of varying applied load (20-180N) and supply pressure (10-60psi).

2. Determination of the dynamic performance of an antagonistic configuration of SPAMs

The response of an antagonistic configuration of SPAMs to a cyclic step response at varying angular displacements (5-30^0) will be analysed to quantify the improved response time compared to the conventional muscle. Secondly, the ability of both types of muscle to recover after an initial angular displacement (5^0, 10^0, 15^0) will be assessed.

3. Integration of supporting hardware into the SPAM design

The structural member of the SPAM design will be modified to house an absolute pressure sensor. The pressure readings taken inside the muscle will then be compared to those taken on the supply line of the muscle (the current default) to determine whether there is a significant difference between the two.

1.2 Methodology

The first part of this project involved the design of an experimental platform that would allow both sleeved and non-sleeved muscles to be tested in the following three configurations:

1. **Isometric:** The length of a single muscle is fixed during inflation.
2. **Isotonic:** The muscle is subjected to a constant load during inflation.
3. **Antagonistic:** The muscles are connected together around a pulley so that the contraction of one muscle rotates the pulley in the direction opposite to that of the other muscle (see Section 2.1).

Similarly, the structural member of the SPAM was redesigned to incorporate an internal absolute pressure sensor as well as the necessary wiring.

Following the design stage, was the construction phase which comprised of the following steps:

- Construction of the experimental rig
- Connecting the valves to the compressor
- Connecting the valves and sensors to the master computer
- Calibration of sensors
- Programming the computer to control the valves and read from the sensors
- Constructing two redesigned SPAMs and two traditional McKibben Muscles

Once the construction phase was complete, the dynamic performance of the sleeved and traditional muscle was first assessed individually and then in an antagonistic configuration.

1.3 Thesis Outline

This report is subdivided into 6 sections, the first of which (Section 1) provides the motivation for the current research, outlines three main objectives, and lists the methods through which these objectives will be achieved.

The opening of Section 2 details the concept and operation of PAMs and gives a brief overview of the historical background before introducing the SPAM design and the many associated benefits. The remainder of this section is devoted to summarising the existing research conducted into improving the physical limitations of PAMs and identifying areas for potential research.

Section 3 describes the setup of the experimental rig and lists the steps that were carried out in each of the tests on both types of muscles. Afterwards in Section 4 and Section 5, the trends evident in the results are stated and discussed before the advances in knowledge of this thesis are summarised in Section 6.

2 Literature Review

The first part of this chapter details the concept and operation of McKibben PAMs (Section 2.1); the development, applications and limitations of the McKibben muscle (Section 2.2); and the concept of the Sleeved Pneumatic Artificial Muscle (Section 2.3). The remainder of this chapter is devoted to explaining the existing methods used to tackle the limitations associated with bandwidth (Section 2.4) and ancillary hardware (Section 2.5).

2.1 McKibben Muscles: Concept and Operation

A traditional McKibben artificial muscle works by inflating an internal bladder, which then presses against an external braided sheath, causing the braid angle to diverge and the muscle to expand radially and contract axially (Figure 2.1) [18,19].

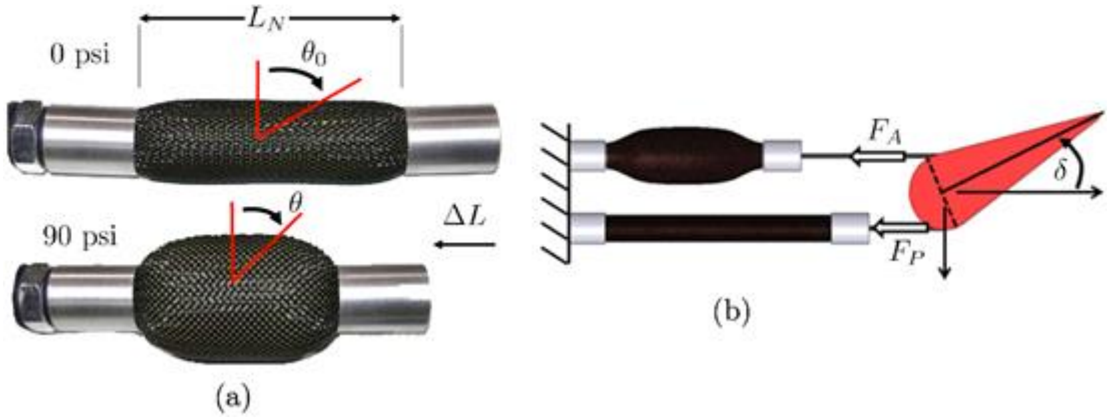

Figure 2.1 a) Illustration of braid angle divergence upon contraction b) Antagonistic setup of PAMs [24]

The bladder is usually constructed of a light, elastic material such as latex [13,18] or silicone [17,25], while the braid is also made from a light but smooth material to easily allow the braid members to slide over one another. In this regard polymers such as PET have shown to be an excellent sheath material [26], however, nylon is the traditional sheath material of the McKibben muscle [8,14,19,20,27]. Kevlar has also been suggested as a possible replacement because of its high stiffness, which mitigates elastic losses [28], however, stiction during contraction is a deterrent that prevents its use [26].

The sheath and bladder are then sealed within rigid end caps [16], through which the muscle is connected to either the supply pressure or the atmosphere by using either two 2/2 valves [6,11,23,29] or single 3/2 valves controlled by Pulse Width Modulation (PWM) [13,22,28,30–32]. Single proportional control valves have also been used [8,20,33–35].

Either a single end cap can be used for both inflating and exhausting the muscle [10,21] or these operations can be split amongst both end caps [11]. Typically the end caps are made of light, structural materials such as aluminium [10,11,14,19,25] because they are also used as fittings to connect with other structural components.

Similar to natural muscle, PAMs are only able to exert a (tensile) force upon contraction, meaning that PAMs must operate in antagonistic configurations [17,30] to allow bi-directional motion of the actuated joint (Figure 2.1 b)).

2.2 Development of the McKibben Muscle

The concept of the McKibben muscle can be traced back to the patent application of Pierce in 1936 who proposed using the radial dilation of an “Expansible Cover” as a replacement for dynamite in the mining industry[10]. It wasn’t until 1949 that the potential of the axial contraction of the “Expansible Cover” was realised by De Haven for use a tensioning device in aviation safety belts. It was at this stage that the artificial muscle inherited its familiar design of the double helical braid surrounding an inflatable bladder [10].

Richard H Gaylord was the first to characterise the muscle and its force output mathematically in his patent for a “Fluid Activated Motor System and Stroking Device” in 1958 [9,10,12,28,36]. It was also around this time that the “McKibben muscle” name was coined because of the work done by the muscle’s namesake Joseph L McKibben in applying the muscle to power orthotics and prosthetics [9,10,12].

The initial interest in the McKibben muscle for orthotic applications was due to the high power to weight ratio [9] and the compliant nature of the muscle, which facilitated a light and safe design. However, the difficulty in controlling a non-rigid actuator [10], the fall in output force with contraction length [9], and the need for heavy pressurised gas tanks [9,10,36] lead to the abandonment of the McKibben muscle in favour of small electric motors and lighter batteries [9,10,36].

From this point onwards robotic system design, particularly in industrial applications, solely consisted of heavy and extremely stiff linkages, powered by strong hydraulic, electric, and pneumatic actuators [23,33,36]. These robust designs facilitated simple control algorithms and mitigated the effects of friction, gravity, and payloads on end-effector accuracy [23,33].

The earliest industrial robots were hydraulically actuated [10,28]. In tandem with internal combustion engines, hydraulic actuators became prevalent in external environments e.g. agricultural, construction, and forestry, due to their ease of control, quick refuelling, and extremely high power and force to weight ratios [10,28]. However, indoor hydraulic systems became obsolete due to oil leaks and excessive noise generation [10,28].

Electric motors are now the dominant actuation method in industrial robotics because their control aspects are well understood and there are a wide range of cheap and quiet models available e.g. ac, dc, stepper [10,23,28]. The improved suitability of electric motors to indoor applications compared to hydraulic actuators comes at the expense of much lower power to weight outputs [28]. Pneumatic cylinders have also found use in industrial applications where simple, high-speed, low-cost, reliable motion is desired but a lack of accurate control and the need for physical end stops limits their applicability[10].

Although, this trifecta of actuation methods has found widespread use in industry the call for compliant actuation methods has seen a resurgence in the popularity of the McKibben muscle. In the 1980s the Bridgestone Corporation launched a variation of the McKibben muscle called ‘rubbertuator’ to imitate natural skeletal muscle and thereby facilitate Human Robot Interaction [9,10,36].

Despite Bridgestone’s discontinuation of the ‘rubbertuator’, many research groups persisted with the McKibben muscle because of its compatibility with human-centred and biomimetic design. The McKibben muscle has since been used in mobile, legged, and service robots to address the shortcomings of other actuation methods [23].

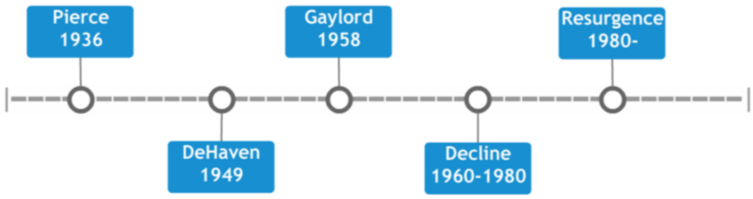

Figure 2.2 Timeline of PAM development

2.2.1 Walking and Running Robots

Walking and running robots designed for dynamic balance, high speed, and smooth motion are best served by compliant actuators which provide shock absorption, low inertia, and potential for energy storage [6,23]. A robotic joint typically requires high torques at low rotational speeds, whereas motors provide low torques at high rotational speeds [23]. Therefore transmissions are required to couple motors to joints and since these transmissions are not backdrivable they not only increase the inertia of the moving joint but also reduce its shock tolerance [23].

The accuracy requirements for walking and running robots is not as rigorous as the industrial world, thereby opening the door for the naturally complaint McKibben muscle [23]. In an antagonistic configuration of PAMs controlling a revolute joint, the angle of the joint is dependent on the difference in the individual muscle pressures, while the stiffness of the joint is equal to the sum of the individual muscle pressures [6,7,33]. Therefore the angle and compliance of the joint can be adjusted independently [6,7].

The availability of compliance as an extra control parameter can be used to make the system robust to external disturbances and to modify the natural frequency for spring-like energy recovery and passive dynamic energy conservation [23,32]. The necessity of a light and portable power source for mobile robotic applications means that electric motors are not an ideal solution. Without access to a mains electricity supply, motors, which are themselves heavy, rely on heavy batteries with long recharge times [6]. Conversely, the McKibben muscle has very high power to weight ratios, ranging from 0.5kW/kg [11] to 10 kW/kg [17], with a lightweight power source that is much easier to store and can be replenished in seconds/minutes[6].

2.2.2 Biomimetic Applications

Industrial robots, consisting of heavy and stiff linkages, excel at carrying out accurate, repetitive movements in highly restricted applications and in confined environments [5]. However, in order to create robots that can robustly perform in uncontrolled and unfamiliar environments it is necessary to adopt the anatomical designs of humans and animals, who have successfully interacted with these environments for millennia.

'The "Biorobotic" approach involves integrating known aspects of neuromuscular physiology and biomechanics into the design of robotic sensors, actuators, circuits and processors, and control algorithms' [5]. The McKibben muscle has contraction ratios (typically from 30-35% [10]), flexibility, compliance, efficiency, bandwidths, control characteristics, and non-linear force-length relationships, all of which are comparable to natural muscle [10–12]. It is for this reason that the McKibben muscle is part of an exclusive set of actuators known as "Pneumatic Artificial Muscles (PAMs)".

Another shared property of both PAMs and natural muscle is that they are stable in open-loop [9,17] i.e. in response to a constant stimulus a PAM will change shape from one equilibrium position to another. This property sets PAMs apart from conventional electric motors (stable velocity for constant current) and fluidic i.e. hydraulic or pneumatic, cylinders, which accelerate under a constant pressure until meeting a hard stop (unstable position and velocity in open loop) [9].

This static stability of PAMs at constant pressure is beneficial with regards to energy consumption because simply closing the muscle valve maintains the joint torque and position without expending any extra energy [17]. The McKibben muscle also features much higher power to weight and force to cross sectional area ratios than natural muscle [10,11]. For example PAMs can produce over $300Ncm^{-2}$ of contractile force per cross sectional area compared to the $20\text{-}40Ncm^{-2}$ achievable by natural muscle [10].

2.2.3 Limitations

Although, the McKibben muscle is the perfect Biorobotic actuator it is not without its disadvantages. The cost of having a light and complaint actuator is that is difficult to model and control [8–10] and will be particularly susceptible to variations in load [28,30] and other disturbances such as shock impacts. Further complicating factors include:

- The properties of the elastomeric materials used to fabricate the internal bladder of PAMs, are heavily temperature dependent [13–16] and will change as the muscle heats up during use [33].
- Frictional effects existing between overlapping sections of helical strands introduces a hysteresis effect[9,16,19].
- The high pressure differences and small valve orifice diameters involved promote turbulence [10,11,20] and choked flow [12,21,22].

Despite all these complications, comprehensive models have been developed that successfully describe the relationship between muscle pressure, length, and output force by incorporating complications such as frictional effects [9,16,36] and choked valve flow [12,21,22].

These theoretical PAM models are then used to determine control signals based on sensor feedback of muscle pressure, length, and force as well as possible environmental variables such as atmospheric temperature. The control algorithms implemented also have an influence on the control signal and can compensate for any errors or simplifications in the theoretical model through tuning or repetitive training.

Consequently, extensive research has gone into developing robust control algorithms that cater for the non-linear system behaviour, hysteresis effects, and load and temperature variations. Early attempts to control the muscles revolved around the use of PID controllers that simply ignored the non-linear effects and thus produced inaccurate position and velocity control [6,20,28,33,35,37].

Modern control strategies for PAMs can be divided into two broad categories [21]:

- Linear control methods that utilise high level computation to adjust control parameters and cater for system nonlinearities
- Nonlinear control methods applied to non-linear models

A summary of the control strategies that have already been applied to PAMs is provided in Table 2.

Simple Linear	**Adaptive Linear**	**Nonlinear**
PID [6,20,28,33,35,37]	Adaptive Pole Placement [13,30]	Sliding Mode Control [21,22,38–41]
	Gain Scheduling [27]	Adaptive Robust Control [42,43]
	Fuzzy enhanced PD+I [15]	Fuzzy [44,45]
	Neural Network enhanced PID [34]	Neural Network [46,47]

Table 2 Control algorithms applied to PAMS

As well as being highly temperature sensitive, the elastomeric materials used to construct the internal bladder are also subject to slow crack growth during cyclic loading, which eventually causes the internal bladder to rupture [5]. As a result, the fatigue limit of PAMs is significantly lower than that of electric motors, fluidic cylinders, and natural muscle [5].

Fortunately, the failure mode of McKibben muscles is well understood. Hannaford and Blake [5] were able to develop an analytical model that could predict the fatigue life of a McKibben muscle via a simple uniaxial tensile test. Furthermore, a number of techniques of extending the fatigue life of the muscle have already been explored and yielded positive results [5,18].

For example, Kingsley and Quinn [18] were able to achieve an order of magnitude increase in fatigue life by pre-stressing the internal bladder and placing a spandex sheath in between bladder and sheath to prevent pinching of the bladder. Additionally, a more tightly woven, less abrasive external sheath allowed the McKibben muscle to withstand up to 14,700 cycles.

It is clear from the preceding paragraphs that the topics of PAM modelling, control, and fatigue life have been thoroughly addressed and as such they will not be considered further in the course of this research project. The focus of this project and the remainder of the literature review is on the physical limitations of PAMs and how they can be addressed.

The following section (Section 2.3) explains the concept of a Sleeved Pneumatic Artificial Muscle and how its unique design can help improve contraction ratio and air consumption.

2.3 Sleeved Pneumatic Artificial Muscles

2.3.1 Concept and Modelling

The modification to the traditional McKibben muscle design necessary to create a Sleeved PAM involves filling the internal muscle cavity with a rigid structural member, which allows the muscle to be self-supporting (Figure 2.3) and the design of the entire actuated system to be more compact [17,48].

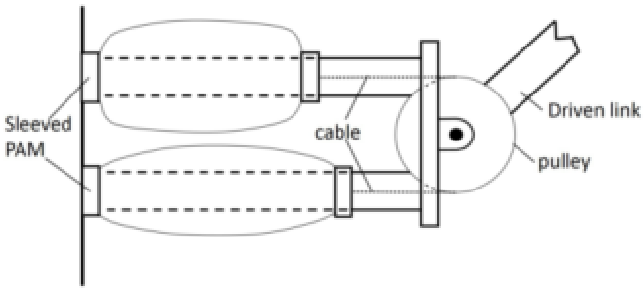

Figure 2.3 Self-supproting sleeved PAM [17]

As shown in Figure 2.4, the cylindrical member is fixed to one end fitting but protruding through the other sealed fitting, thereby allowing this perforated fitting to slide along the central shaft as the muscle contracts. Replacing the volume V_1, which would otherwise push against the end fittings when pressurised and oppose the contraction of the muscle, with the structural member increases the muscle force capacity and contraction ratio. Furthermore, a reduction in air mass consumption and pressure required to generate a given force, is facilitated by the smaller internal volume required to be pressurized.

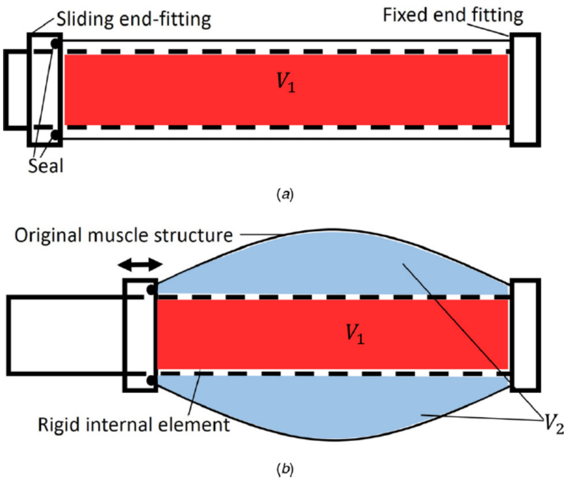

Figure 2.4 Internal volume removed by the structural member [17]

The explanation provided in the previous paragraph can be verified formally using the following relation developed by Chou and Hannaford [20],

$$F = -P' \frac{dV}{dL} \tag{1}$$

where P' is the gauge pressure in the muscle, V is the internal muscle volume, and L is the muscle length. As is stated by Equation 1, a decrease in length (negative dL) accompanied by the coupled increase in volume (positive dV) will produce the (positive) contractile force characteristic of the McKibben muscle.

Considering both Equation 1 and Figure 2.4, it is clear that the volume V_2 provides the (positive) increase in overall volume, dV, which is then counteracted by the (negative) decrease in volume V_1. Applying this same logic to the SPAM, it becomes apparent that the absence of the volume V_1 leads to a greater increase in the total volume dV and hence the contractile force. The volume removed by the addition of the structural member and the increase in contractile force for any muscle length are given by [17],

$$\Delta V = -\left(\frac{L\pi {D_1}^2}{4}\right) \tag{2}$$

$$\Delta F = P'\left(\frac{\pi {D_1}^2}{4}\right) \tag{3}$$

where L is the current muscle length and D_1 is the diameter of the cylindrical member.

2.3.2 Experimental Performance

The constant force increase for any muscle length was verified experimentally by Cullinan et al. (at a constant pressure of 410kPa) and is demonstrated in Figure 2.5 a). Additionally, Figure 2.5 b) illustrates how the reduction in internal volume reduces the pressure required to produce a given force (500N). The reduction in pressure is most prominent at high contraction ratios, where the constant force increase (given by Equation 3) becomes increasingly significant as the output force of the muscle drops.

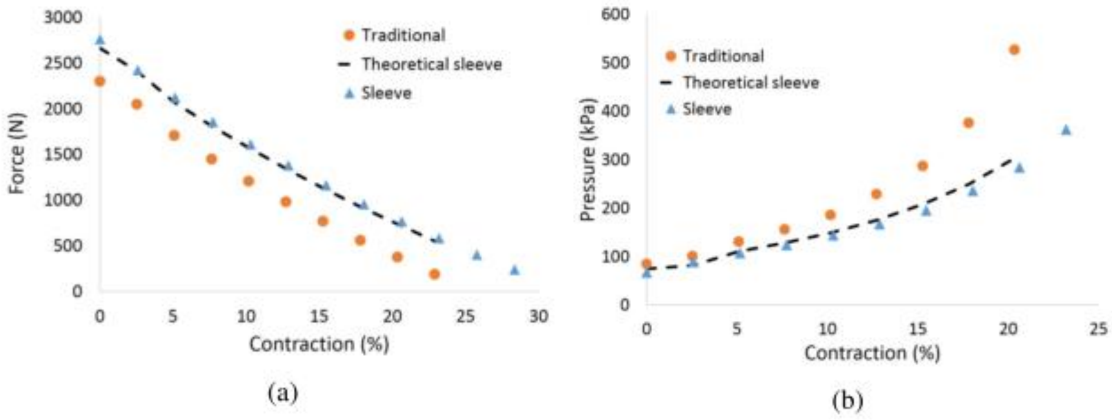

Figure 2.5 a) Increased force output and b) Decreased pressure requirement of the SPAM [17]

Similarly, the increasingly prominent ΔF leads to a greater pneumatic energy saving at large contraction ratios. On the other hand, at small contraction ratios the volume saved by the sleeved adaption and the associated reduction in air mass consumption is at its greatest. Once again, this phenomenon was verified experimentally by Cullinan et al., yielding a maximum energy saving of 47.7% at 0% and 17.5% contraction, and a minimum energy saving of 24.5% at 10% contraction (Figure 2.6).

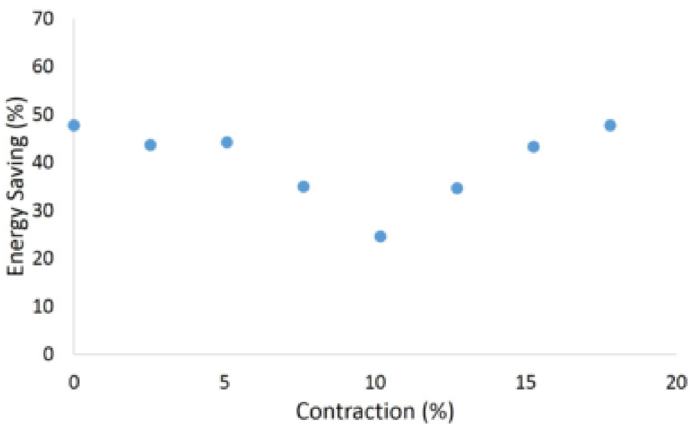

Figure 2.6 SPAM energy saving compared to a traditional McKibben muscle at 500N [17]

2.3.3 Summary

The sleeved adaptation conceived by Driver and Shen has been proven to address some of the problems with traditional McKibben muscles, while also introducing the ability for the muscle to support load. Both the experiments of Driver and Shen, and Cullinan et al. showed a constant increase in force output across the entire contractile range and a reduction in pressure required to produce a given force, verifying the theoretical predictions [17,48].

Moreover, the sleeved design of Cullinan et al. achieved a pneumatic energy saving from 24.5-47.7%, improving on the equivalent 20-37% of Driver and Shen, and a 5% higher contraction ratio compared to traditional muscles.

Aside from establishing the benefits for contraction ratio, air consumption, and force output neither Cullinan et al. nor Driver and Shen have explored the effect of a reduced muscle volume on the SPAM response time. The following section (Section 2.4) is devoted to investigating the methods employed by other researchers to quicken muscle response and to applying these insights to the sleeved design.

2.4 Bandwidth

The bandwidth of PAMs is considered to be too low for practical applications [10], resulting in poor tracking performance and response times because the muscle cannot inflate and deflate quick enough to match the demands of the reference input. Below is a summary of the existing research in the literature to address the bandwidth limitations of PAMs.

2.4.1 Modelling

Chou and Hannaford [20] model the air flow inside the PAM using well established equations from analogous electrical circuits.

The muscle volume (V) is modelled as a capacitance (C_A) and expressed as [10],

$$C_A = \frac{V}{RT} \tag{6}$$

where R is the universal gas constant, T is the temperature of the air.

The difference between the supply and the internal muscle pressure is treated as the voltage driving the flow of air against the viscous losses encountered in the peripheral valves and piping. Using the pneumatic equivalent of Ohm's Law yields [10],

$$Q = \frac{P_s - P}{R_T + R_s} \tag{7}$$

where Q is the air flow rate, P_s is the supply pressure, P is the internal muscle pressure, R_T represents the losses from the valve and the valve-muscle piping, R_s represents the losses from the air source and the source-valve piping.

The previous two equations can be incorporated into the expression for the circuit cut off frequency (f_c) of a "low pass pneumatic filter" as follows [10],

$$f_c = \frac{1}{2\pi(R_T + R_s)C_A} = \frac{QRT}{2\pi(P_s - P)V} \quad (8)$$

Analysis of the above equation describing the bandwidth of the system confirms the expected outcome that increasing the flow rate to the muscle and decreasing the internal muscle volume will allow for faster filling and emptying, and therefore greater response times.

2.4.2 Maximising Flow Rate

The diameters and lengths of tubing used in PAM applications typically present a much smaller obstruction to the flow than the small orifice diameter of the pressure control valves [10]. Therefore, although Poiseuille's Law indicates that increasing the pipe diameter and decreasing the pipe length will increase the flow rate [11], Equation 7 illustrates that the resistance associated with the valve (R_T) will become the limiting factor.

In order to address this limitation, a logical step would be to use multiple valves in parallel with as large an orifice diameter as possible. The effect of the increased flow rate achieved by the parallel valve configuration can be included in the bandwidth equation by dividing the valve resistance by the number of valves present [10],

$$f_c = \frac{1}{2\pi(\frac{R_T}{N_V} + R_s)C_A} \quad (9)$$

The experimental tests carried out by Davis et al. (Figure 2.7) showed an approximate 400% increase in bandwidth, for both the isotonic (200N loading) and isometric conditions, upon increasing the valve number from 1 to 8.

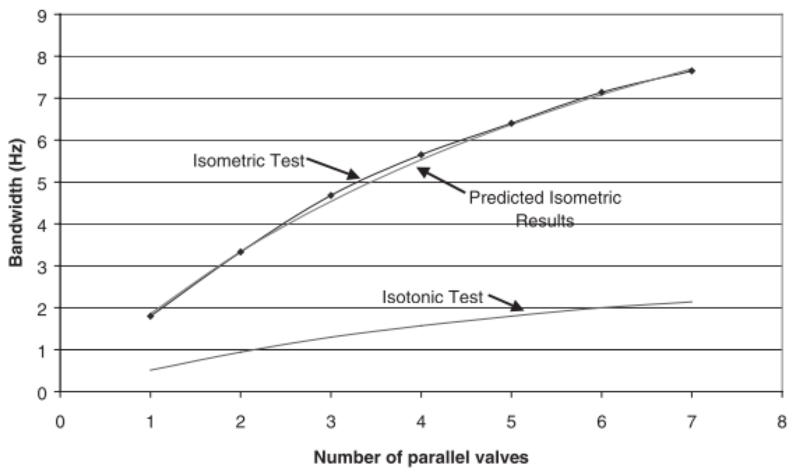

Figure 2.7 Effect of valve number on Isometric and Isotonic performance [10]

There are also a number of simple steps to increase bandwidth such as increasing the supply pressure, minimal use of pipe connectors, addition of air reservoirs near the valve input, and maximising muscle inlet bore diameter [10,20].

Unfortunately, the increase in flow rate derived from a larger orifice is compromised by the associated increase in valve size and mass. Similarly, a multiplicity of valves will also increase the peripheral weight as well as increasing the energy consumption of the system. Although there are methods available to mitigate the effects of valve mass (Section 2.6.1) and energy consumption (Section 2.6.3), a much more elegant approach involves decreasing the internal volume of the muscle itself.

2.4.3 Minimising Internal Volume

It is clear from Equation 8 that smaller muscle volumes will have higher bandwidths. However, the decreased size of the muscle leads to a lower contractile force [10], thereby introducing the challenge of decreasing the internal volume yet maintaining the muscle size.

The internal volume of the muscle solely serves to contain the pressurized air acting radially on the braided sheath, which in turn gets converted to longitudinal motion. Therefore, the pressurised air is the driving force, not the internal volume, meaning that so long as the pressure is maintained within the muscle, the internal volume can be decreased. Accordingly, pressurising the smaller internal volume will be quicker, yielding a faster response time, while also lowering the air mass consumption of the muscle.

Davis et al. [10] proposed the use of three fillers to decrease the dead space inside the muscle. They suggested that the optimum filler should fill the maximum amount of space possible without restricting air flow, yet be incompressible and light to minimize the added mass.

i) **Granular:** The addition of small (5mm length and 2mm diameter) oval shaped granules to the muscle cavity produced a peak 50% increase in bandwidth when 55% of the internal volume was occupied. It is believed that at fill levels above 55% the obstruction of the granules to the air flow outweighs the beneficial decrease in internal volume, producing the decline in performance evident in Figure 2.8.

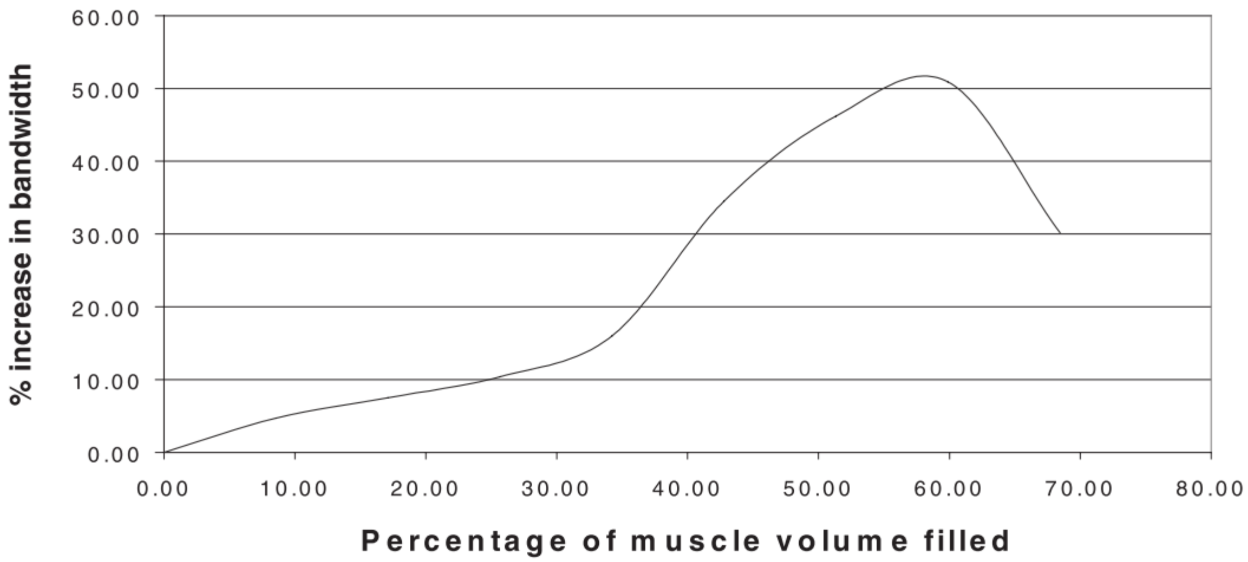

Figure 2.8 Increase in bandwidth versus granular fill percentage [10]

ii) **Solid:** Solid rods of diameter equal to the minimum muscle diameter were cut into short lengths and inserted into the muscle one at a time. Analysing Figure 2.9, it is noticeable that the solid filler achieved a 5 times higher bandwidth increase than the granular filler but is still subject to a sharp decline in performance, due once again to flow restriction.

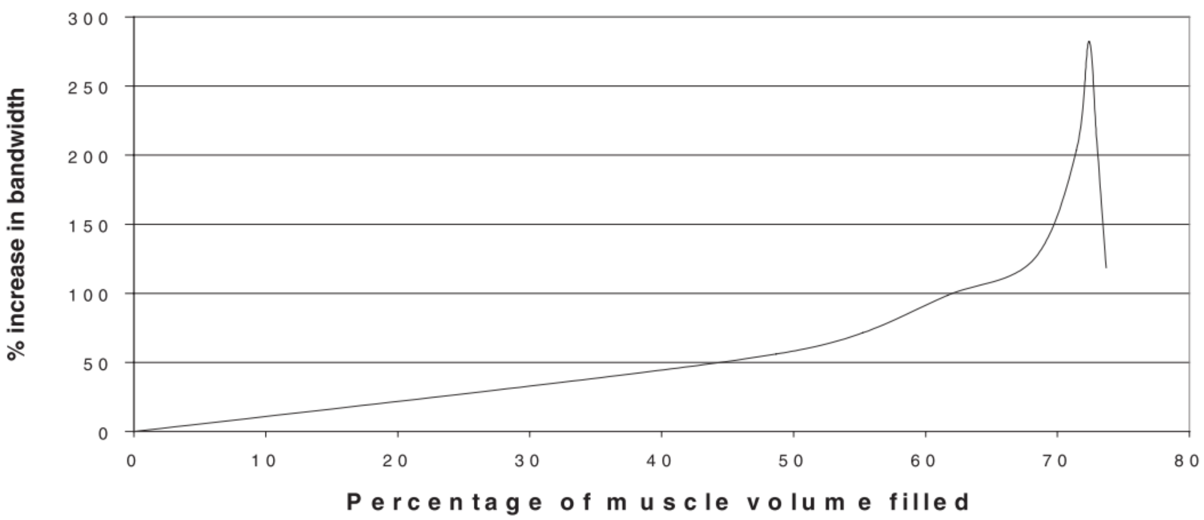

Figure 2.9 Increase in bandwidth versus solid fill percentage

iii) **Liquid:** The ability of water to redistribute itself, mitigated obstruction to the flow of air, leading to a monotonic increase in bandwidth, approaching 400% (Figure 2.10). The exponential increase in bandwidth is similar to the solid filler pre-decline, and as shown in Figure 2.10, Equation 10 can be used to accurately model this exponential rise [10],

$$\%increase\ in\ b_w = \frac{Fill_{vol}}{Act_{vol} - Fill_{vol}} \tag{10}$$

In order to prevent water escaping from the valves during deflation of the muscle, an elastic sheath was used to contain the water inside the muscle yet still allow the natural distribution of water to occur.

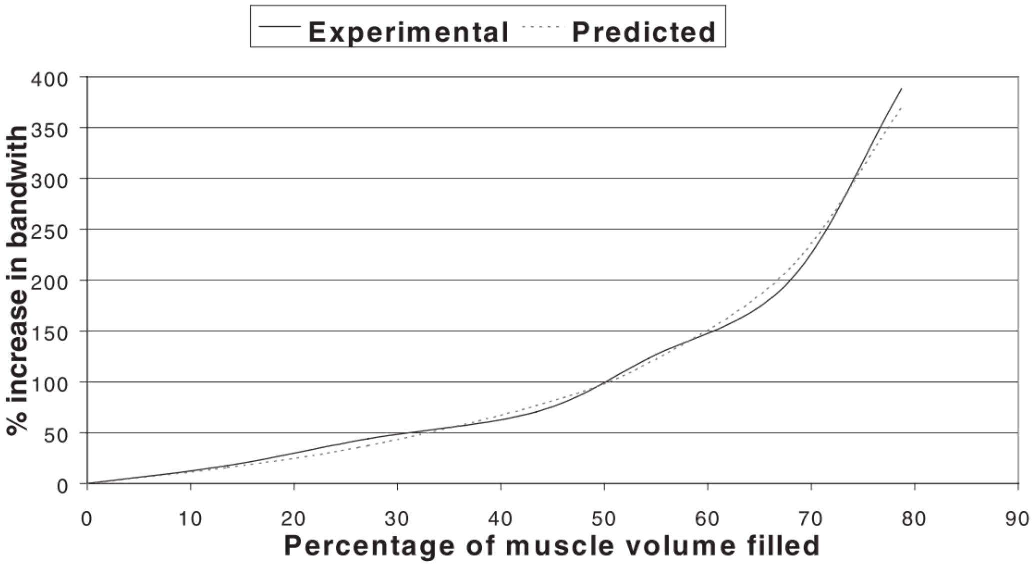

Figure 2.10 Increase in bandwith versus liquid fill percentage [10]

All of the previous graphs were obtained under isometric conditions for a single McKibben muscle, however, PAMs must be used in antagonistic configurations due to their unidirectional force output. Accordingly, Davis et al. carried out isotonic tests to assess the impact of filler volume and flow rate on the bandwidth of an antagonistically actuated revolute joint, the results of which are included in Table 3.

Flow Rate $(l/s)^{-1}$	Volume Filler (ml)	Bandwidth (Hz)
1.5	0	0.6
1.5	200	0.9
3	0	1.2
3	200	1.5

Table 3 Bandwidth performance of an antagonistic configuration in response to fill volume and flow rate [10]

Comparing the tests with and without filler, it is clear that doubling the flow rate with and without the filler results in a 67% and 100% increase in bandwidth, respectively, whereas including the filler for flow rates of 1.5 and 3 l/s causes a 50% and 25% increase, again respectively. The first trend in the previous sentence could be due to the added mass of the filler compromising the advantage of the decreased volume, while the second trend suggests that filler flow restriction becomes more problematic for larger flow rates.

It is noticeable that the number of tests carried out for the antagonistic configuration is quite limited, and therefore this sample is not sufficient to confirm the relationships derived from the results of Table 3. Consequently, there is potential for further work in verifying these two trends by testing a broad range of fill percentage and flow rate combinations for an antagonistic configuration. The improvements of these fillers on the contraction ratio, air consumption, and force output has already been explored via the sleeve muscle design [17,48], however the effect of filler mass on power to weight ratio and joint stiffness still needs to be established.

2.4.4 Hybrid Actuation

An alternative approach to increasing the actuator bandwidth is to use a combination of electric motors and PAMs, as was done in the construction of the robotic arm in Figure 2.11 [35]. The arm features a small electric motor attached to the arm using low-friction, low-reduction cable transmission to compensate for the low bandwidth of the PAMs.

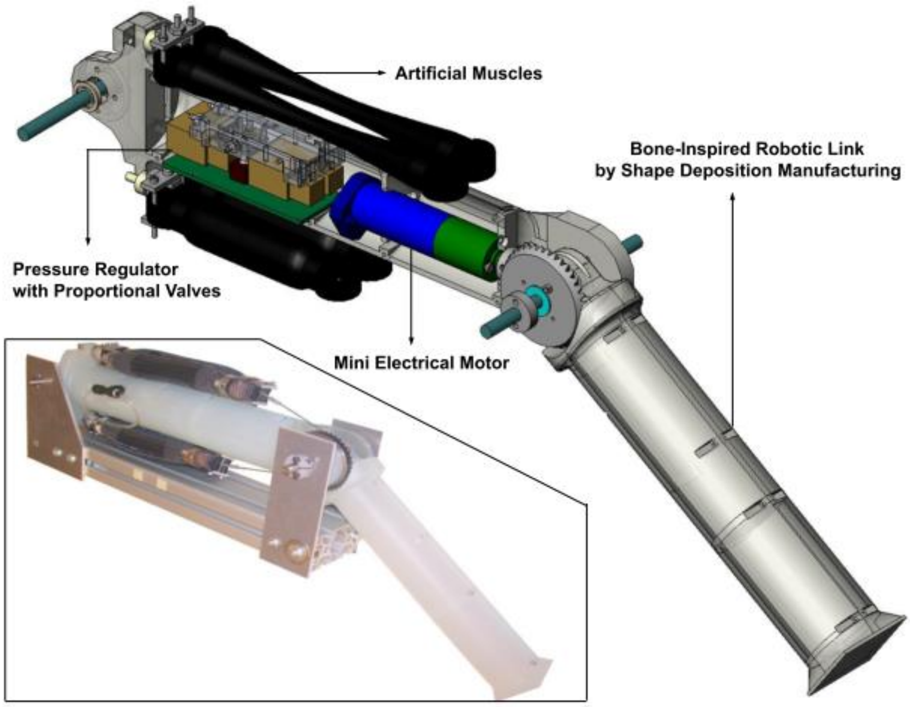

Figure 2.11 2nd generation S2p Stanford Safety Robot [35]

The control algorithm employed divides the reference input torque based on frequency content such that the low frequency torque is delegated to the PAMs (Macro), while the high frequency torque is delegated to the fast acting electric motor (Mini) [35,49]. Consequently, this strategy ensures that the majority of the actuator's power comes from the lightweight PAMs, while the small electric motor merely tops up the power in the high frequency range. Overall this allows for a lightweight but responsive robotic arm.

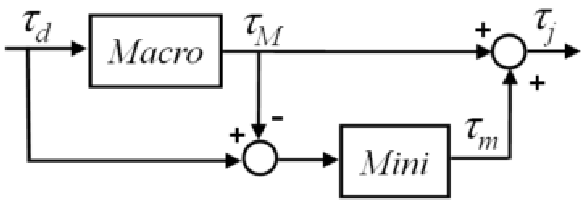

Figure 2.12 Closed loop feedback diagram for hybrid actuation [35]

The open loop contact force test revealed that the hybrid actuation approach yielded a bandwidth of 26Hz compared to the 6Hz achieved by the PAMs acting alone (Figure 2.13 a)). Furthermore, the addition of the electric motor more than halves the positional tracking error for a 10 degree, 6Hz sinusoidal input (Figure 2.13 b)).

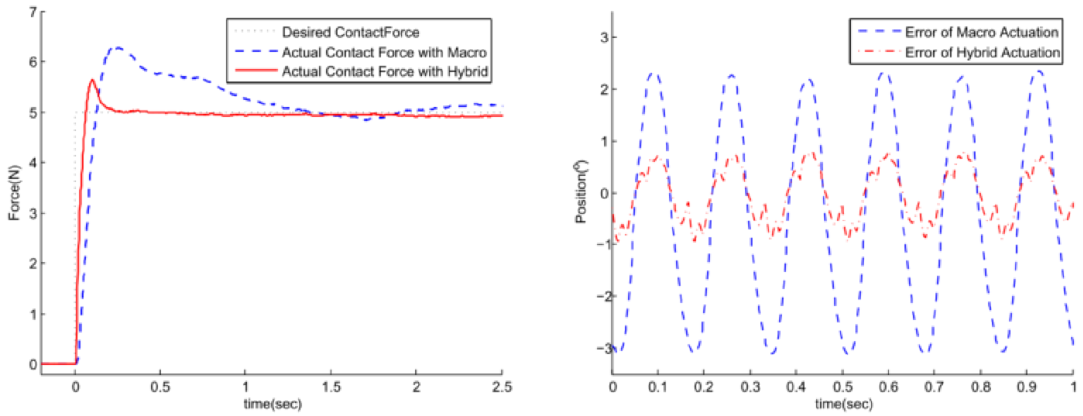

(a) Contact Force Control (b) Position Control Error

Figure 2.13 Macro versus hybrid control [35]

2.4.5 Summary

The work of Davis et al. suggests that the sleeved design should offer a substantial increase in muscle bandwidth, however, as of yet this has not been experimentally verified for a single SPAM or an antagonistic SPAM configuration. Furthermore, the influence of the structural member mass on power to weight ratios and joint stiffness is still unknown.

The additional mass of the structural member is not a major concern, as it allows the muscle to be self-supporting and means an antagonistic configuration of SPAMs could easily become a limb of a humanoid robot. Therefore, although the sleeved design may be heavier it compensates by removing the need for additional load bearing members that would otherwise add a similar amount of weight to the system if a traditional muscle were used.

What is more of a concern, is the added mass and space requirement of peripheral hardware such as the valves and sensors needed to control the muscle, but as shown in the next section (Section 2.6) these problems can be offset by incorporating this hardware into the actuated limbs themselves.

2.5 Ancillary Hardware

The merit of PAMs as biomimetic actuators breaks down once the peripheral hardware that is needed to support PAM operation is considered. The additional mass provided by the valves raises the power needed to actuate the muscle, reduces the power to weight ratio, and increases the risk of injury from potential collisions.

Comparing Table 4 and Table 5 it can be seen that the mass of the valves and the volume that they occupy is comparable to and can even be many times greater than the mass and volume occupied by the PAMs themselves. The average valve and PAM volume calculated from the aforementioned tables are 144cm^3 and 155cm^3, respectively. Similarly, the average valve and PAM mass are 365g and 363g, respectively.

Based on this evidence it is clear that strategies need to be employed to reduce the mass of the overall system, in order for the PAM to maintain its status as a lightweight and compact actuator.

Type	Mass (g)	Length (mm)	Diameter (mm)	Volume Occupied (cm^3)	Author
Traditional McKibben	5.5	90	10	7.1	[28]
Traditional McKibben	10.5	79	12.7	10.5	[13]
Traditional McKibben	59	140	31.8	112.6	[8]
Pleated	100	100	25	49.1	[6]
Festo MAS-10-N-220-AA-MCFK [50]	146.7	220	10	17.3	[34]
Festo MAS-40-N600-AA-MCKK [50]	1398	600	40	754.0	[43]
FESTO DMSP-20-150N-RM-CM [50]	195.7	150	20	47.1	[21]
Sleeved McKibben	990	195	40	245.0	[17]

Table 4 Compilation of different PAMs used by other authors

Also sensors are required to obtain readings of muscle pressure, output force, and contraction length so that the PAMs can be controlled in closed loop. If the electric energy consumption of these ancillary sensors and valves is high then heavy batteries must be incorporated into the design, further detracting from the veracity of the lightweight power source ideal.

	Matrix 820 [51]	KV Automation Microsol [52]	Joucomatic Piezotronic [53]	Matrix 750 [54]	Festo MPPE-3-1/8-10-010-B [55]	Festo MPYE-5-1/8HF-710-B [56]	Festo MPYE-5-M5-010-B [56]	Festo MPP-3-1/8 [57]
Port/Channel	2/2	2/2	2/2	8 Block 2/2	2/2	5/3	5/3	5/3
Type	PWM Solenoid	PWM Solenoid	Piezoelectric	PWM Solenoid	Proportional	Proportional	Proportional	Proportional
Valve to muscle ratio	2	2	2	0.25	2	0.5	0.5	0.5
Mass [per valve, per muscle] (g)	25,50	30,60	32,64	340,86	710,1400	330,165	290,145	950
Dimensions (mm)	37x28.5x12	47x15x21	48x25x15.2	55x55x48	129.1x62x38	149.3x45x26	129.9x45x26	146.5x50x45
Volume Occupied (cm^3)	12.7	14.8	18.2	145.2	304.2	174.7	152.0	329.6
Power (W)	0.8-2.9	1-2	0.004	1.4-1.9	3.6	33 (max)	33 (max)	17.4
Flow Rate (L/min)	100-180	120	7	50-100	375	700	100	1200
Pressure Range (bar)	0-8	0-16	0-4	0-8	0-1	0-10	0-10	0-10
Response Time (ms)	1-5	10-15	8-15	2-5	-	-	-	25-30
Orifice Diameter (mm)	-	3.6	-	-	5	6	2	-
Lifetime (million cycles)	500	100	-	500	-	-	-	-
Authors	[6,23]	[11]	[11]	[11]	[8]	[34]	[21]	[20]

Table 5 Compilation of valves used by other authors

2.5.1 Actuator Integration

An approach that has proved popular involves the incorporation of ancillary hardware into the actuated joint or the end caps of the muscles. The actuated joint of the first generation of the S2ρ robotic arm (Figure 2.14), mimics the design of human bone but has an internal vacancy, which is used to house the electric motor for hybrid actuation (Figure 2.15).

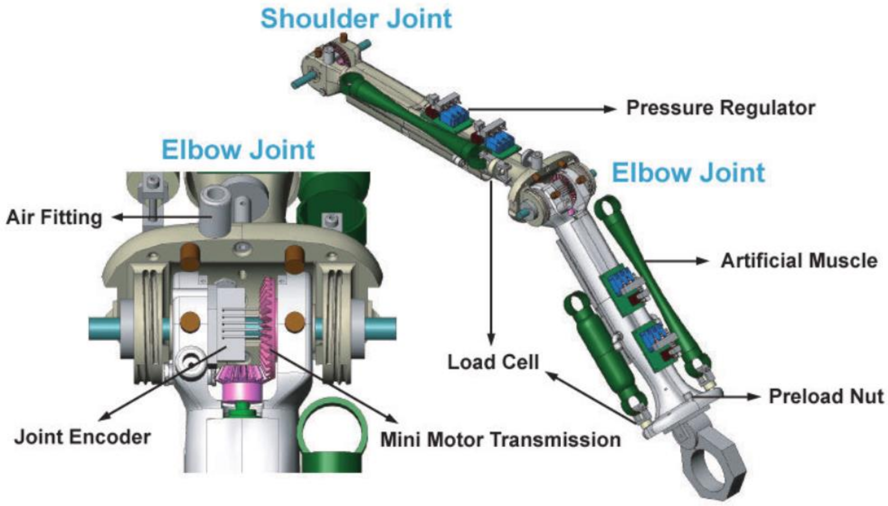

Figure 2.14 1st generation Stanford Safety Robot [49]

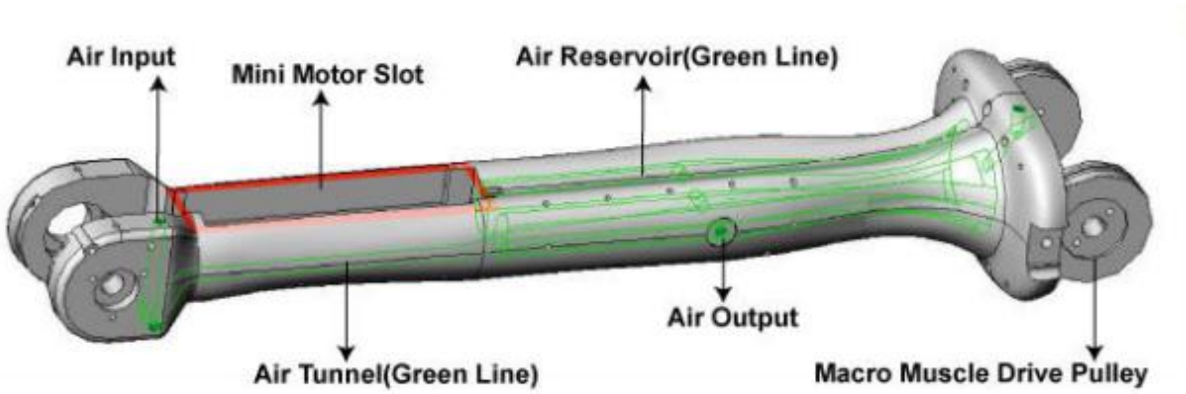

Figure 2.15 Close up, isolated view of the bone-shaped robotic link [49]

The volume of bone removed to form the slot reduces the mass of the overall system and the position of the motor along the central axis, adjacent to the joint (on the far left) improves the balance of the limb and reduces the torque required for motion. Similarly, the use of 3D manufacturing techniques (Selective Laser Sintering [35] or Solid Deposition Manufacturing [58]) enables the centre of the bone to be hollowed out and an airline to be created to the valves. This integrated air distribution system reduces the mass of the bone and removes the need for external piping, without compromising on bending strength.

The pneumatic valves are situated directly on top of the bone and are connected directly to the air distribution system, making the design more compact and increasing the muscle bandwidth by reducing transport pressure losses [49]. Looking at the elbow joint of the arm it can be seen how the pulleys from the bone are used as an attachment point for the lower arm, which is actuated by connecting cables to these pulleys from the muscles in the upper arm.

The creators of the S2ρ arm state that SDM will allow future versions of the arm to not only incorporate mechanical components but also electronic power sources and sensors.

The work of Davis et al. [11], also features a number of methods to integrate valves and sensors but more impressively this integration is achieved solely within the muscle end caps and internal bladder. The design of Davis et al. placed a Microsol solenoid valve (by KV Automation Systems [52]) directly in the end cap of the muscle (Figure 2.16), producing a 26% weight reduction in overall mass compared to using external Matrix 750 valves [54].

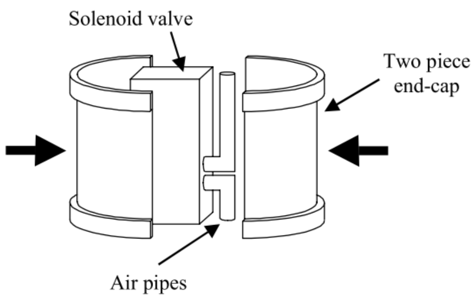

Figure 2.16 Solenoid valve mounted in the centre of a two piece end-cap [11]

However, the 30% reduction in flow rate by having to use the Microsol valves small enough to fit in the end caps, means that the overall power to weight ratio remains unchanged but that the response time of muscle will be significantly reduced. Despite the setback, this modification still eliminates transport pressure losses from valve to muscle and raises the force to weight ratio of the muscle by 26%. These advantages warrant work into developing a custom, two-in-one valve and end fitting design that will allow for increased orifice diameters.

2.5.2 Sensor Integration

Pressure

An alternative use of the muscle end cap is to house a pressure sensor (Figure 2.17) [11,23]. The location of the pressure sensor inside the end cap removes the need for tubes and fittings between the valve and muscle, allowing for a lighter and more compact design [11,49].

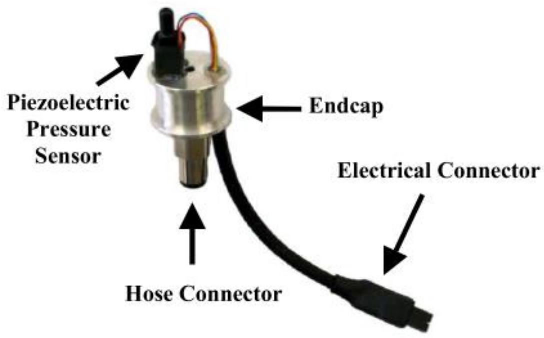

Figure 2.17 Piezoelectric pressure sensor mounted in the actuator end cap [11]

According to Poiseuille's Law the pressure loss, ΔP, of laminar flow in a pipe due to viscous dissipation is given by [11],

$$\frac{\Delta P}{Q} = \frac{8L\eta}{\pi r^4} \tag{11}$$

where Q is the flow rate, L is the pipe length, r is the pipe radius, and η is the viscousity. It is clear from Equation 11 that the further apart from the muscle the pressure sensor is and the smaller the pipe diameter, the greater the discrepancy between the actual pressure in the muscle and the value returned by sensor. Therefore the collocation of pressure sensor and muscle will reduce head loss, improve flow rates and bandwidths, and provide more accurate readings and closed loop control.

Torque

One method of incorporating torque measurement into the system design is by mounting strain gauges on the spokes of the pulleys actuated by the PAMs [59], however precise machining is required to produce these internal, radial spokes. A more practical approach is to place strain gauges on the end caps to measure the tensile force generated by each muscle (Figure 2.18) [11], which when combined with the knowledge of the pulley diameter allows the joint torque to be calculated [60].

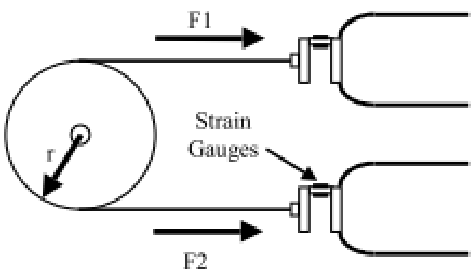

Figure 2.18 Joint torque measurement via end cap mounted strain gauges [11]

Contraction

The simplest, but least accurate method (errors of up to 5% [11]), of determining the contraction of the muscle is by inputting measured force and pressure data into an analytical model because once two of these three variables is known the third can be calculated. Instead of opting for expensive and stiff Linear Variable Differential Transformers (LVDT), Davis et al. offer a number of low cost, rapidly constructed alternatives that can directly, and therefore more accurately, measure muscle contraction.

All three of the methods suggested; Strain Gauge (+/- 2mm accuracy), Rotary Potentiometer (Figure 2.19), and Resistance Wire (<0.5mm accuracy), were able to be contained within the internal bladder of the muscle, allowing for a more compact design.

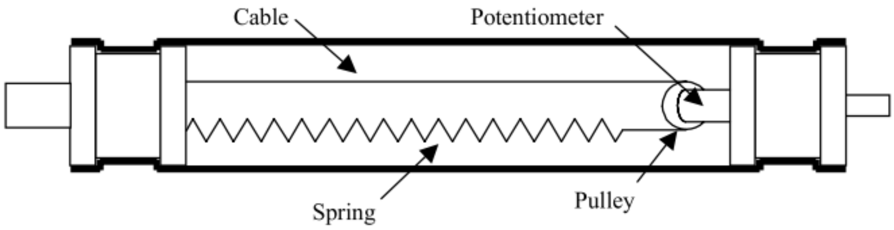

Figure 2.19 Contraction measurement using a rotary potentiometer [11]

2.5.3 Electrical Energy Consumption

As mentioned previously the power requirements of the valves is a concern, particularly for mobile robotics platforms with limited energy supplies [32]. For example the Microsol and Matrix 750 valves used by Caldwell, require 1.2W and 1.9W respectively, but there are methods available to reduce the power requirement of solenoid valves [61] significantly.

Piezoelectric valves were also explored by Davis et al. due to their extremely low power consumption, 24mW in the case of the Joucomatic Piezotronic valve used by Davis et al. However, the poor flow rate of 7 L/min, ten times less than the Matrix 750 valves, meant that the only feasible way to utilise this valve was through a pneumatically actuated poppet switch.

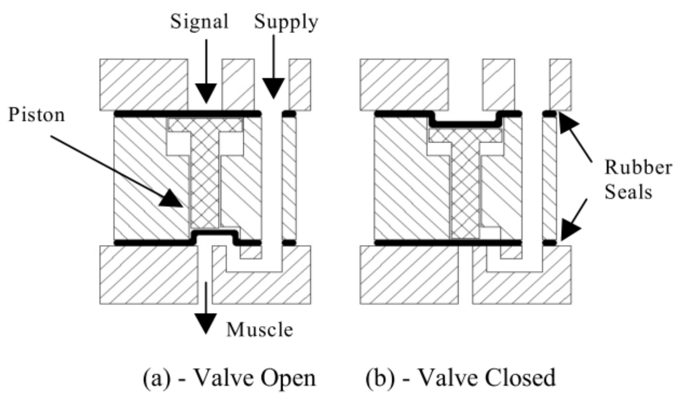

Figure 2.20 Poppet design [11]

The signal is connected to the supply pressure through the piezoelectric valve, so that when the Piezoelectric valve is opened flow to the muscle will stop, due to the larger piston area over which the signal pressure acts. Conversely, when the Piezoelectric valve is closed the air in the right passage, at the supply pressure, will force the piston upwards and subsequently enter the muscle.

The incorporation of the poppet switch into the end cap, means that the piezoelectric valve is just used as a trigger, thereby leveraging the low power requirement (1.2% of the Matrix 750 power requirement) while still maintaining reasonable flow rates through the larger orifice diameter of the passage on the right. Despite the larger flow rates achieved by the right passage they were still 33% less than the Matrix 750 valves, which when combined with the 60% increase in switching times lead to a slower response times (Figure 2.21).

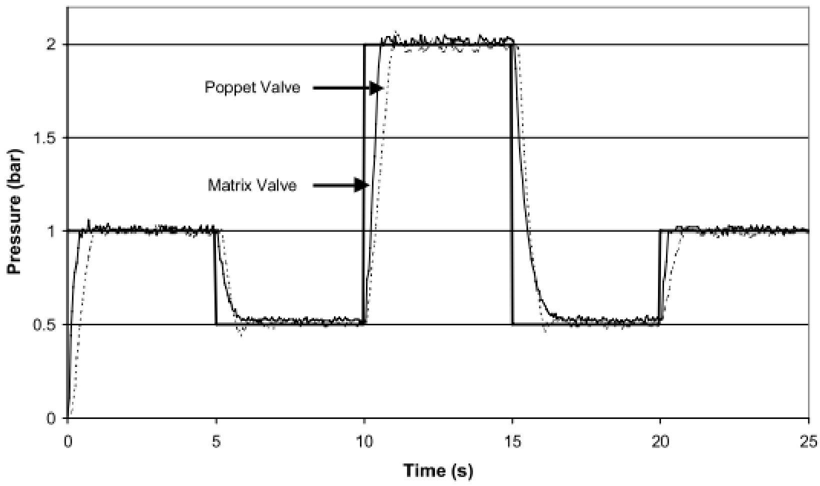

Figure 2.21 Step pressure response for Matrix and poppet valves [11]

There are alternative poppet valves available such as the Hoerbiger P8 poppet valve that can deliver high flow rates (110 l/min at 600kPa) using minimal power (5.8mW). However, these valves weigh 120g each and since 2 valves are required for each muscle this will added 240g to overall system weight, which would completely remove a PAM's merit as a lightweight actuator.

The dynamic performance of the poppet valve was also analysed (Figure 2.22). At both frequencies the slope of the decline (muscle deflating) is significantly lower than the incline (muscle inflating). This is because the pressure driving the poppet piston upward and inflating the muscle is the supply pressure minus the muscle pressure, whereas the driving pressure for the exhaust valve is the lower muscle pressure, which decreases as the muscle deflates.

This effect was also witnessed by other authors [6,23,49]. In Vanderborght's case [23] a 7 bar supply was used with a maximum muscle pressure of 3 bar, meaning that the minimum pressure difference of 4 bar across the inlet valve was even greater than the maximum pressure difference of 3 bar across the outlet valve.

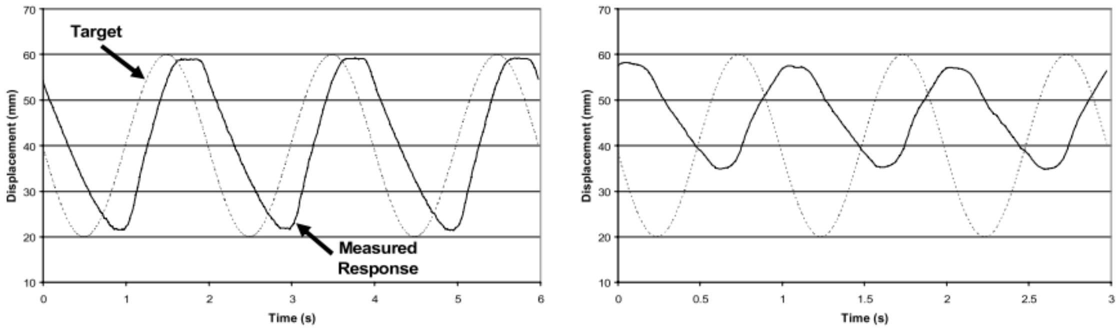

a) b

Figure 2.22 Poppet valve tracing a) 0.5Hz and b) 1Hz sinusoidal input [11]

As a result inflating the muscle is always faster than deflating the muscle when using valves with the same orifice diameter. This discrepancy is most visible at a frequency of 1Hz where the slower exhaust rate limits the minimum displacement of the muscle to roughly 35mm instead of the intended 20mm. The lower poppet driving force of the exhaust valve is also manifested through the plateaus of the peaks, which indicate the delays associated with this lower driving force overcoming the stiction of the rubber seals [11].

Not only does this asymmetric flow rate decrease the output range, it can also cause oscillation of the PAM [49]. Therefore, the number of exhaust valves to inlet valves is doubled to balance the inflation and deflation times [6,23,49], however this is not an elegant solution as it increases mass and energy consumption. The findings of this subsection (Subsection 1.4.2) provide further motivation for the development of a customizable valve design that will allow exhaust valves to have larger orifice diameters than inlet valves.

2.5.4 Summary

The novel ideas for hardware integration presented in this section optimise the entire PAM system in terms of weight, size, and efficiency. However, a lot of the aforementioned concepts cannot be readily applied to a SPAM because of the presence of the internal structural member. Therefore an interesting challenge for this project is applying this integrated hardware approach to the unique design of the SPAM.

This section (Section 2.6) also identified the lack of flexibility of commercial valves and illustrated the need for a modular, customizable valve design. It is evident that being able to change the valve orifice diameter is an important consideration. It is hoped that additional features of an ideal PAM valve will be identified throughout the course of this project and thus form the foundation for future work in this area.

The following chapter (Chapter 3) accumulates the points of interest arising from this literature review and outlines the research that will be undertaken in this project to address the unanswered questions arising from these points.

2.6 Research Motivation

The McKibben muscle shows excellent promise as an anthropomorphic actuator yet practical limitations have so far prevented wide scale use in robotics. Its characteristic compliance and an increased demand for human-robot interaction mean that it is worthwhile researching methods to address these challenges and improve performance.

In this regard, the sleeved adaptation of the McKibben muscle has been shown to offer significant reductions in air consumption (up to 48%) and pressure requirements, while increasing force output and contraction length (5% increase). However, the dynamic characteristics of this actuator have not yet been examined.

The increase in bandwidth achieved by Davis et al. [10] through the use of filler materials bodes well for the SPAM, but this has not yet been experimentally validated. This information is important in order to formulate effective dynamic models of the SPAM and enable effective control, especially at high bandwidths. This gap in the literature forms the foundation of this thesis.

Focusing on the peripheral hardware of PAMs, it is evident that the integration approach adopted by Davis and Caldwell [11] and Shin et al. [35,49] is an effective way to produce a more compact, lightweight, accurate and energy efficient system. Therefore, a secondary objective of this research is to apply the techniques implemented by these authors, on traditional McKibben muscles, to the unique design of the SPAM.

The following Section, details the design of an experimental rig and the testing procedure used to determine the response time of the SPAM for isometric, isotonic, and antagonistic setups.

3 Experiment Setup and Procedure

3.1 Testing Apparatus

3.1.1 Design Requirements

In order to be able to successfully quantify the dynamic performance of both muscles, an experimental rig needed to be designed and constructed to meet the following design requirements:

- Configurable for both single and antagonistic muscle testing
  - Allow length of single muscle to be fixed during inflation (Isometric)
  - Provide constant load during single muscle inflation (Isotonic)
  - Provide a means to couple two muscles in an antagonistic fashion
- Allow for testing of the muscles in a vertical (aligned with gravity) and horizontal (aligned transverse to gravity) orientation
- Accurate force, pressure, and contraction measurement for up to two muscles
- Facilitate pneumatic actuation of the muscle
- Readily adaptable for muscles of different length
- Rigid for minimal deflection under high muscle forces (>2000N)

3.1.2 Frame

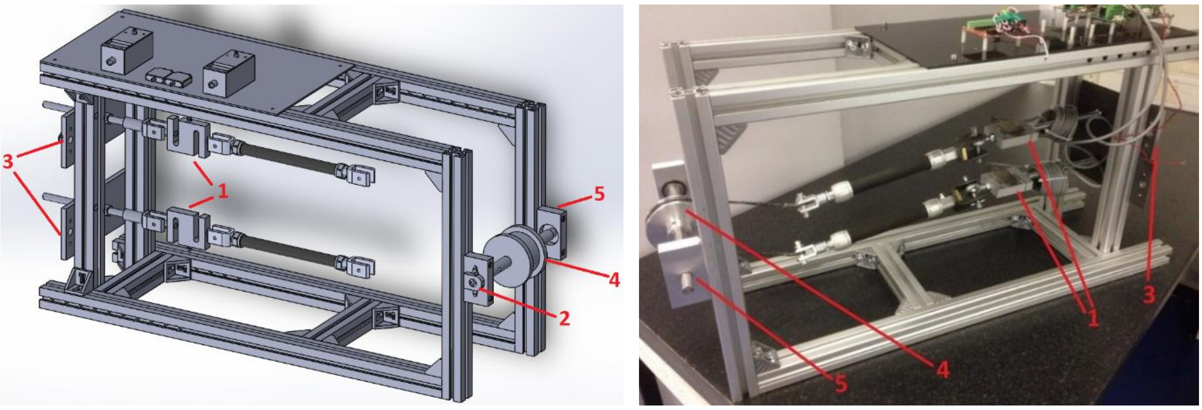

a) b)

Figure 3.1 a) CAD model of the experimental rig b) Actual experiment rig

The experimental rig was constructed out of Aluminium extrusion and fitted together using sliders so that the constituent frame members can be easily moved around and swapped out. As is illustrated later in this section, the configurability of the rig design allows the muscles to be tested in either the horizontal or vertical orientation and in either an isotonic, isometric, or antagonistic setup.

Other noteworthy features highlighted in Figure 3.1 include:

1. Load cells to measure the force generated by the muscles
2. An encoder to measure the angular displacement of the joint.
3. Steel endplates to hold the muscles and load cells in place.
4. Pulley
5. Pillow blocks supporting either end of the pulley support

A valve scaffold was introduced to support the valves and pressure sensors connecting to the inlet of each muscle (Figure 3.2) and a lever arm was added adjacent to the pulley so that the antagonistic configuration could be tested under load.

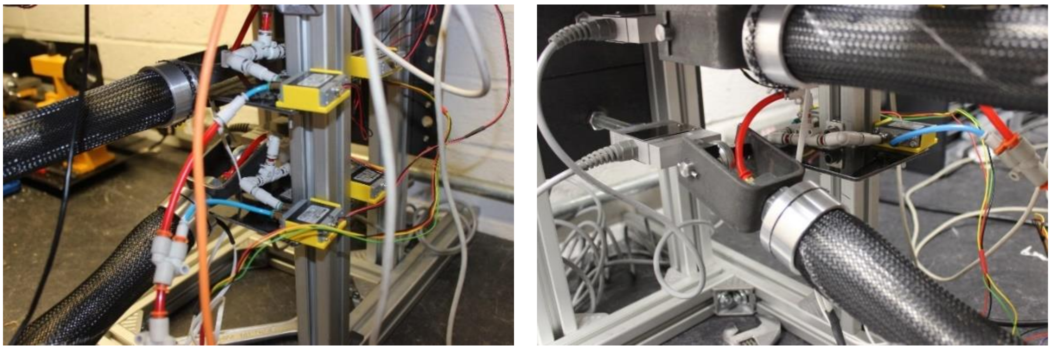

Figure 3.2 Valve scaffold

Figure 3.3 Lever arm

3.1.3 Electronic Hardware

The electronics needed to monitor the muscle response variables i.e. pressure, force, as well as supply pressure and joint angle revolved around using an Intel Mini ITX motherboard to interface with the necessary sensors over their respective communication protocols (Figure 3.4). This PC was also responsible for actuating the valves via an Arduino and MOSFET breakout board.

Label	Description
PSU	Power Supply Unit
MX87QD	Intel Mini ITX Motherboard MX87QD [62]
DVI	PC DVI Port
Valve Arduino	Arduino for PWM control of valves
Load Cell and Load Cell CAN	Mantracourt DSC Strain Gauge [63]
Encoder Arduino	Arduino to read encoder values
Mux	NXP PCA9544A: 4-channel I2C-bus multiplexer [64]
MOSFET V-04	4 Route MOSFET IRF540 V4.0 [65]
Pressure Sensor	Honeywell Tru-Stability HSCDANN150PG2A5 [66]
Valve	Matrix 721 2/2NC [67]
Encoder	CUI AMT20 Absolute Encoder [68]

Table 6 List of electronics used on the experimental rig

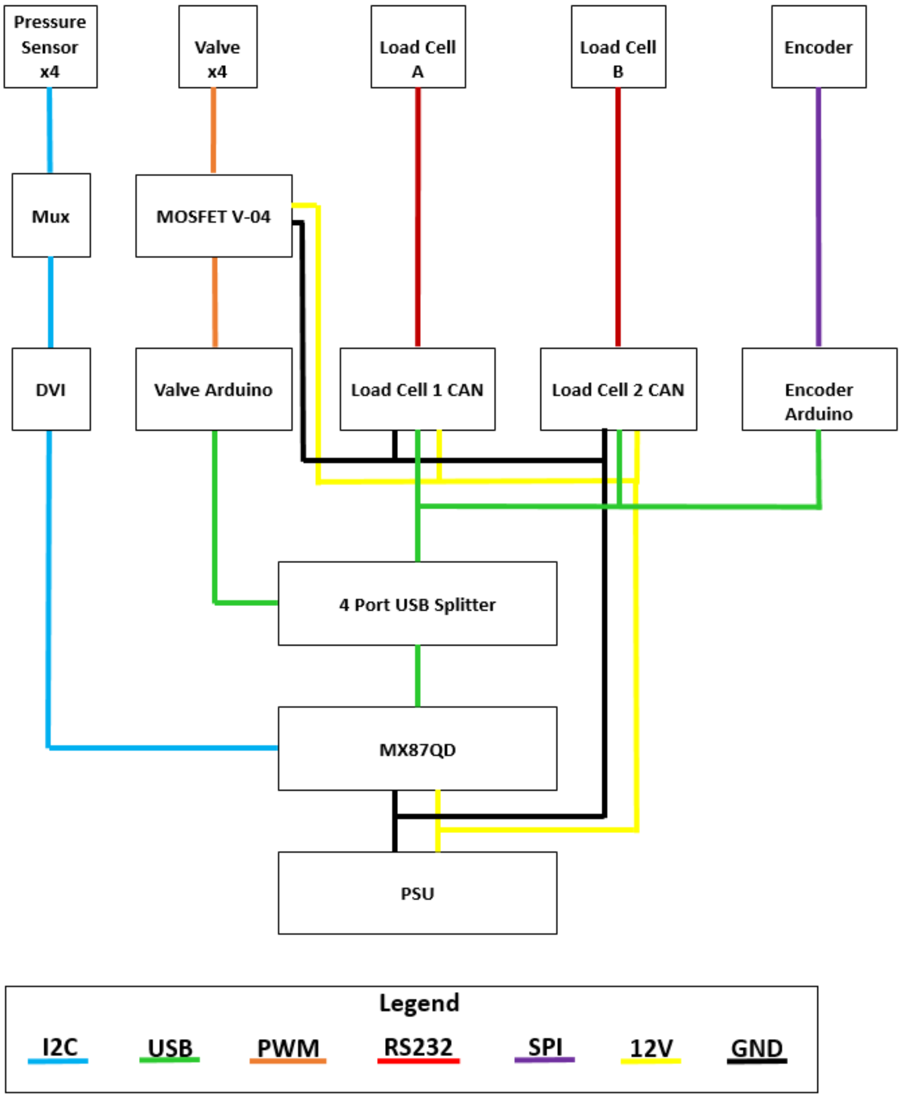

Figure 3.4 Electronic schematic

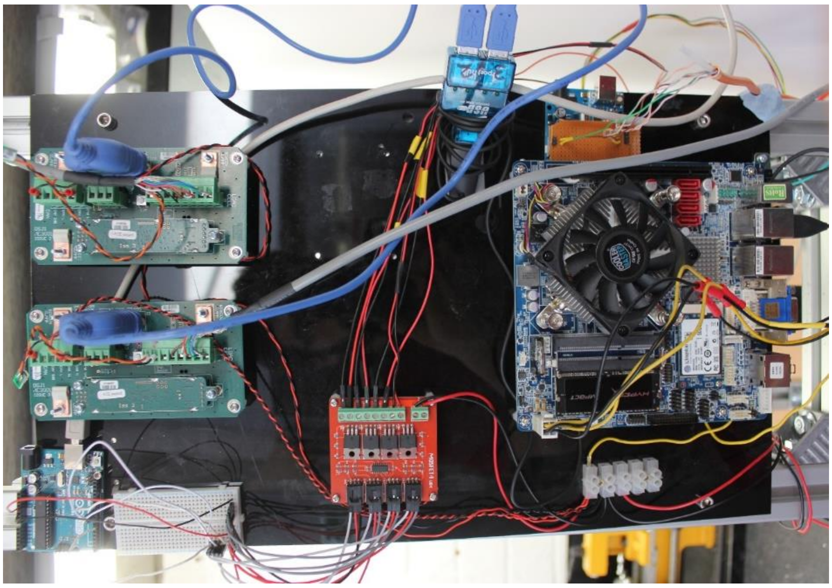

Figure 3.5 Top view of the electronic components

3.1.4 Pneumatics

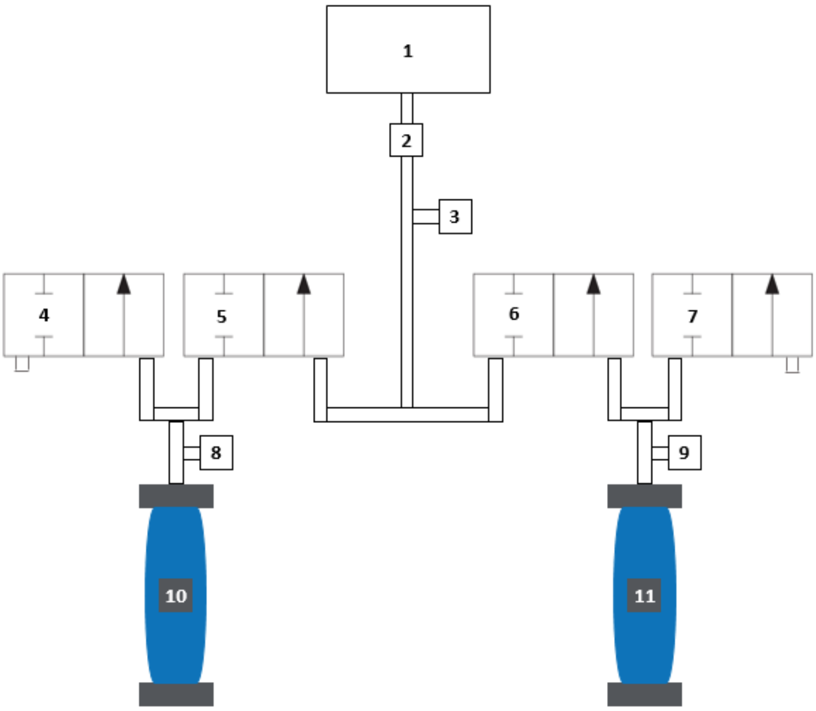

Figure 3.6 Pneumatic diagram from compressor to muscles

Label	Description
1	MGF SIL-EOL 50/100 CAR Compressor [69]
2	AW G30 – F02G1H Pressure Regulator [70]
3	Supply Pressure Sensor
4	Exhaust Valve Muscle A
5	Inlet Valve Muscle A
6	Inlet Valve Muscle B
7	Exhaust Valve Muscle B
8	External Pressure Sensor Muscle A
9	External Pressure Sensor Muscle B
10	Muscle A (with optional Internal Pressure Sensor)
11	Muscle B (with optional Internal Pressure Sensor)

Table 7 List of pneumatics used on the experimental rig

3.1.5 Code Architecture

The code used for every experimental test relies on the 6 threads which run in parallel as a particular test program executes:

1. The log thread writes all the sensor values to a file every 2ms.
2. The pressure thread sequentially switches channels on the multiplexor to read from all of the active i2c pressure channels.
3. The Load A thread continuously reads the force generated by muscle A.
4. The Load B thread continuously reads the force generated by muscle B.
5. The encoder thread continuously reads the angular displacement of the pulley.
6. The main thread is used to send the valve commands needed for a particular test and it displays live sensor readings to the PC monitor.

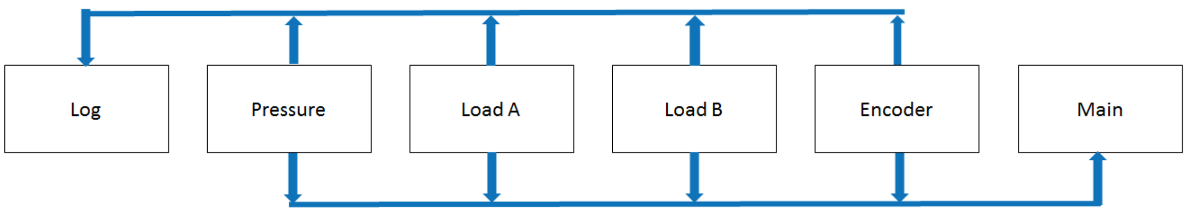

Figure 3.7 Multithread architecture for every test program

3.1.6 Pressure Sensor Integration

To accommodate the absolute pressure sensor inside the sleeved muscle a recess had to be machined into the length of the structural member and a hole drilled from this recess to transport the wires out towards the endcap (Figure 3.8). A slot also had to be cut into the endcap to allow the four wires to lie below the top surface of the endcap which would be tightened to the central member using an M20 nut.

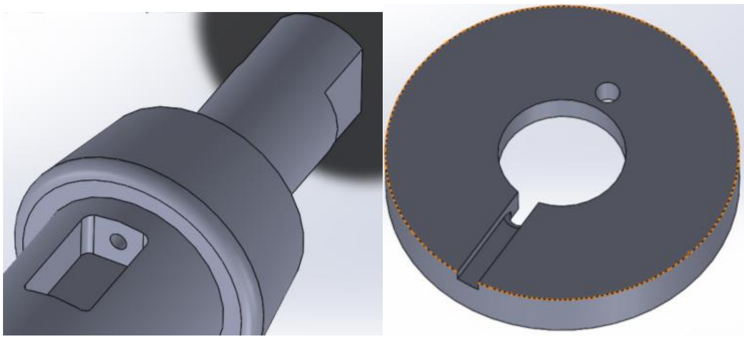

Figure 3.8 Recess machined into the structural member (LHS) and the slot milled into the endcap (RHS)

Once the structural member had been prepared the pressure sensor was then fixed to the structural member using non-conductive epoxy resin (Figure 3.9). The resin also acts as a seal preventing air from escaping through the hole drilled in the recess.

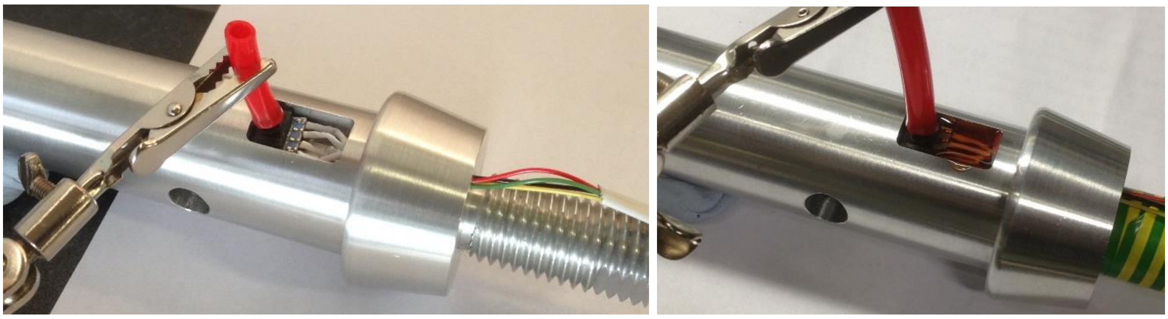

Figure 3.9 Fitting of the pressure sensor to the internal element before addition of epoxy resin (LHS) and after addition of epoxy resin (RHS)

3.2 Experimental Procedure

3.2.1 Isotonic Step Response

The aim of this test was to subject the muscle to a constant force during inflation by attaching it to an applied load through the pulley. Ideally when the muscle contracts the pulley will rotate freely, the mass will rise uniformly, and the muscle will be subject to constant force equal in magnitude to the weight of the load. However, as is illustrated in Section 4.2.1 there are significant inertial effects which detract from the isotonic assumption.

1. Setup the experimental rig in the vertical orientation with one end of the muscle secured to the load cell and the other secured to the weights via the dyneema rope (Figure 3.10).
2. Set the pressure on the regulator to 10psi.
3. Place the smallest weight on the weight stand.
4. Run the “Isotonic.c” program on the PC, which opens the inlet valve of the muscle for 10s, closes the inlet valves, waits 1s, and then opens the exhaust valve for

another 10s. This program also logs the muscle pressure, muscle force, supply pressure, and encoder angle at 2ms intervals for the duration of the test.

5. Repeat step 4 until the test has been carried out at every weight level.
6. Repeat steps 3-5 at 10psi increments until 60psi.

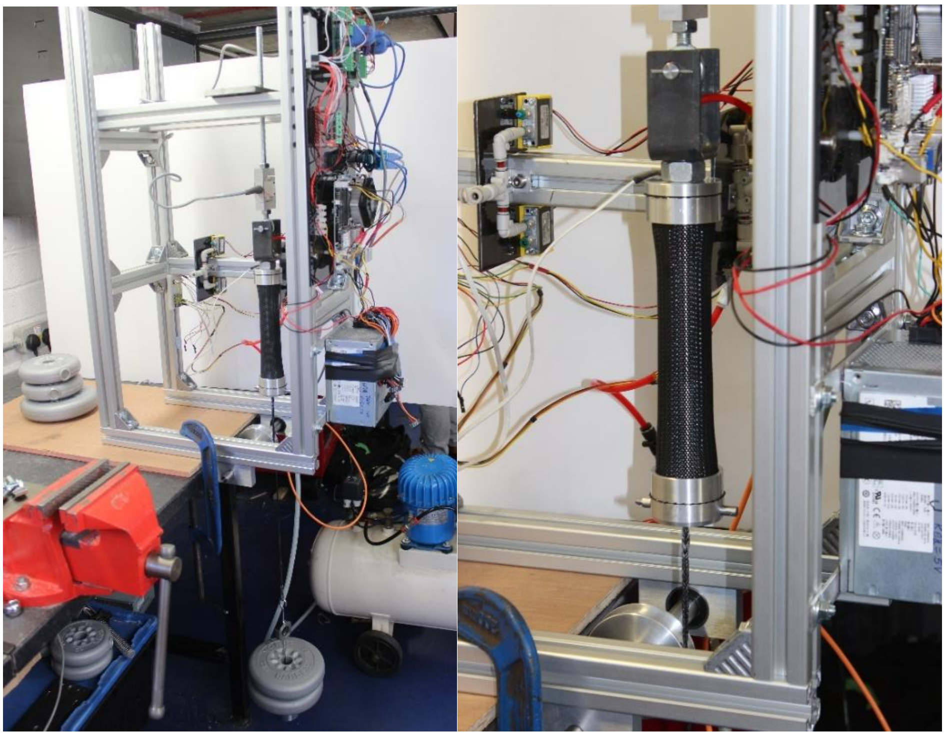

Figure 3.10 Isotonic setup for the SPAM

3.2.2 Isometric Step Response

The aim of this test was to inflate the muscle while keeping its length fixed. The vertical orientation of the rig was chosen so that gravity acts along the axial direction of the muscle. In the horizontal orientation the non-sleeved muscle would sag substantially and would have to oppose gravity as it inflated. On the other hand the SPAM was supported by its central member and was not afflicted in this way and hence the horizontal orientation would not have provided a fair comparison. Before the test began the load cells were zeroed so that the self-weight of the muscle acting on the load cells was removed.

1. Setup the experimental rig in the vertical orientation with either end of the muscle secured to load cells, which are in turn attached to the steel end plates at the top and bottom of the rig.
2. Tighten the nuts on either side of the top endplate until there is approximately 40N of pretension on the muscle.
3. Measure this initial length of the muscle and the length to which the top steel bolt protrudes through the endplate (Figure 3.11).
4. Set the pressure on the regulator to 10psi.
5. Run the “Isometric.c” program on the PC, which opens the inlet valve of the muscle for 10s, closes the inlet valves, waits 1s, and then opens the exhaust valve for

another 10s. This program also logs the muscle pressure, muscle force, supply pressure, and encoder angle at 2ms intervals for the duration of the test.

6. Repeat step 5 at 10psi increments until 60psi
7. Feed a length of steel bolt equal to 5% of the initial muscle length past the end-plate (it is easier to measure the contraction of the muscle indirectly like this) and repeat steps 4-6.
8. Repeat steps 4-7 for up to 25% contraction in 5% increments.

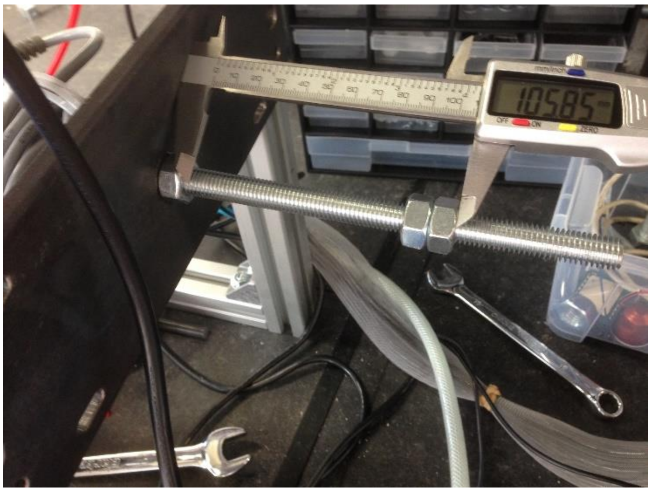

Figure 3.11 Measuring the contraction of the muscle indirectly

3.2.3 Antagonistic Step Response

As mentioned previously, PAMs must be setup in an antagonistic configuration to facilitate controlled bi-directional motion. Since bi-directional motion is most often desired in robotics applications, it was imperative that both muscles be tested in this configuration. Consequently, this test was concerned with getting the pulley to undergo cyclic angular step responses so that the average response time could be established over a number of cycles.

1. Setup the experimental rig in the horizontal orientation with two muscles coupled in an antagonistic configuration through the pulley using the Dyneema rope (Figure 3.12).
2. Measure the initial length of the un-inflated muscles.
3. Inflate both muscles to half of the supply pressure for the test (60psi in this case) and measure the contraction.
4. Tighten the nuts on either side of both endplates until the contraction of both muscles is half of the initial contraction measured in step 3.
5. Set the pressure on the regulator to 60psi.
6. Place the lightest mass on the lever arm.
7. Run the “Antagonistic_Step.c” program on the PC passing in “5” as the argument. This will cause the lever arm to undergo ten oscillations between the $+5^0$ and -5^0 position while simultaneously recording the muscle pressures, muscle forces, supply pressure, and encoder angle at 2ms intervals for the duration of the test.

8. Repeat step 7 passing in values from 10-30 in increments of 5 as arguments to the program.
9. Repeat steps 7 and 8 for all available weights.

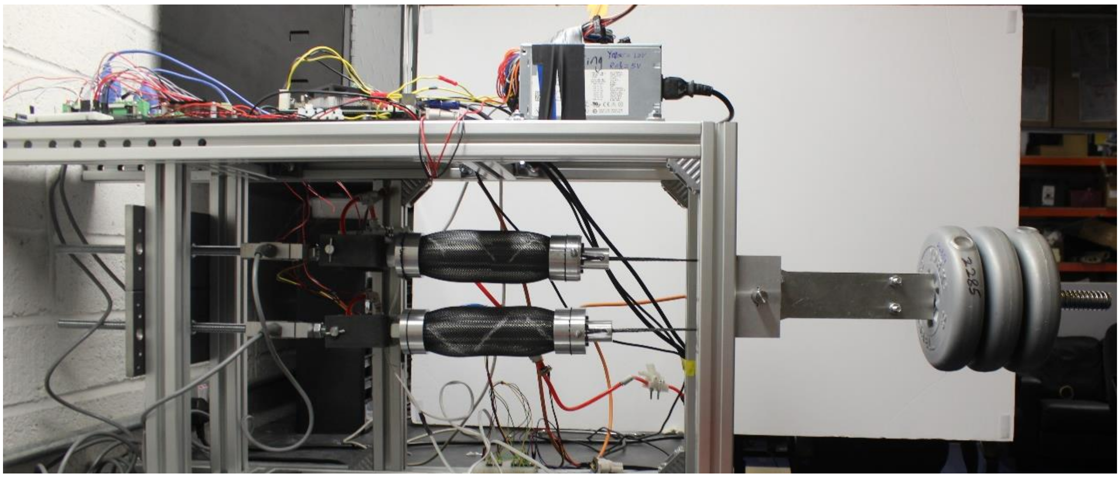

Figure 3.12 Antagonistic setup of the SPAM

3.2.4 Antagonistic Disturbance Test

An important consideration for control of robotic linkages is how they will behave when subjected to an external disturbance. Therefore, the aim of this test was to compare the ability of the two muscle types to recover from initial angular displacements in terms of settling time, number of oscillations, and overshoot.

1. Setup the experimental rig in the horizontal orientation with two muscles coupled in an antagonistic configuration through the pulley using the Dyneema rope (Figure 3.12).
2. Apply the lightest weight to the lever arm.
3. Run the “Disturbance.c" program on the PC, which will bring the lever arm to the neutral position and record the muscle pressures, muscle forces, supply pressure, and encoder angle for the duration of the test.
4. Once the arm is at the neutral position, manually lift the lever 15^0 above the neutral position using the feedback from the encoder on the PC monitor.
5. Hold this position steady for 3 seconds.
6. Release the mass and wait for the oscillations to die away.
7. Repeat 3-6 for an initial displacement of first 10^0 and then 5^0.
8. Repeat 2-7 for all available weights.

4 Results

4.1 Isometric Step Response

4.1.1 Individual Step Response

In order to evaluate the Isometric response of the sleeved and non-sleeved muscles, the pressure rise time was determined for 10-60psi over a 0-25% contractile range. An example of the typical output from one of these tests for the non-sleeved and sleeved muscles are shown below in Figure 4.1 and Figure 4.2 respectively.

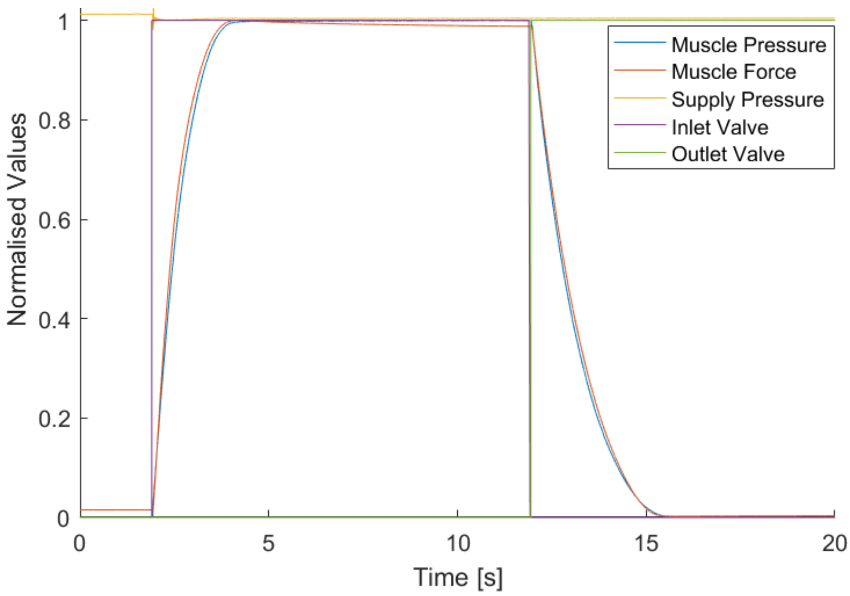

Figure 4.1 Normalised response variables for normal muscle at 0% contraction and 60psi

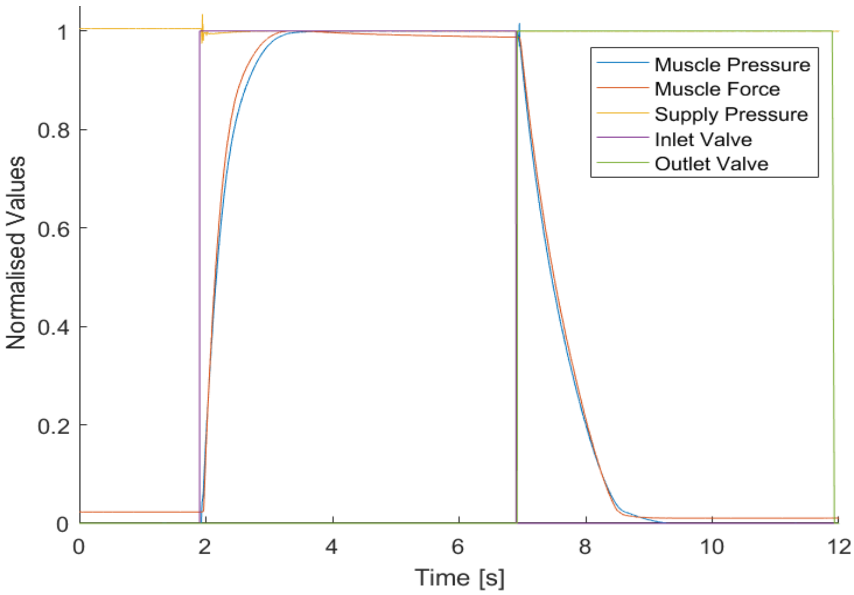

Figure 4.2 Normalised response variables for sleeved muscle at 0% contraction and 60psi

Considering the normalised response plots (Figure 4.1 and Figure 4.2) it is clear that there is no appreciable delay between the opening of the inlet valve and the rise in muscle pressure. Initially the rise of the pressure is at its greatest due to the large pressure differential between the muscle and supply tank, which gradually reduces, leading to a corresponding decrease in the rate of pressure increase. Comparing these normalised plots to the individual pressure response plots (Figure 4.3 and Figure 4.4) it is noticeable that although the supply pressure drops upon opening the inlet valve it stabilizes rapidly and therefore still provides a steady reference pressure. It is this steady reference pressure which is quoted as the target pressure in Figure 4.11 and Figure 4.13.

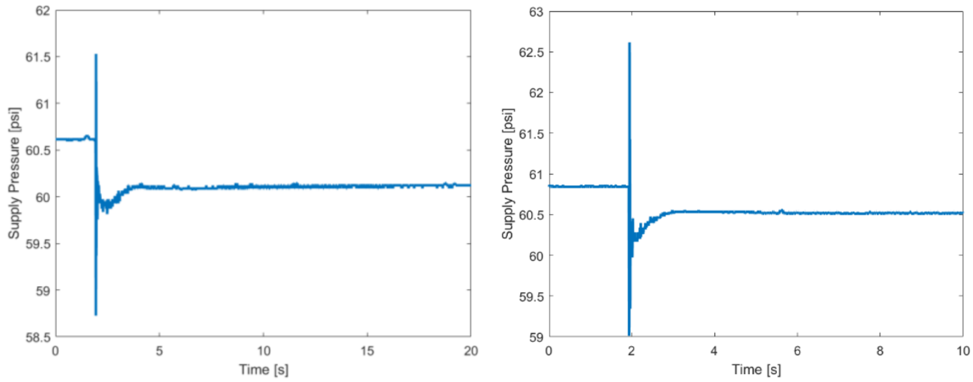

Figure 4.3 Supply pressure step response for non-sleeved (LHS) and sleeved (RHS) muscle at 0% contraction and 60psi

In isometric tests, the induced muscle force is approximately proportional to the muscle pressure [71,72], hence the step response of these two variables are coupled to one another and the choice to measure either step response should be arbitrary. However, the choice of muscle pressure instead of force as the response variable to establish rise time was implemented because the pressure does reach steady state, whereas the force does not(Figure 4.4 and Figure 4.5).

The reason for this is due to the braid of the muscle slipping out from the end caps leading to a gradual reduction in force. Furthermore, at large contraction ratios the muscle force can be seen to dip initially before rising upwards, which would have a significant effect on rise time calculations (Figure 4.6 and Figure 4.7). Initially as the muscle is inflated the pressure acting axially on the end caps pushes out against the load cells causing a negative compressive force. Then, as the braid angle diverges and the muscle expands radially outward, the tensile force generated overcomes the compressive force, causing the net force to rise with pressure monotonically thereafter.

This phenomenon is most prevalent at high contraction ratios and low pressures (Figure 4.6 to Figure 4.8). Of course the sleeved muscle suffer less from this effect due to the fact that the majority of the central cylindrical volume between the endcaps is occupied by the rigid member and thus the area over which the pressure can act over the endcaps is reduced.

Only tests where the muscle was able to exert a tensile force were taken into consideration for rise time calculations meaning that tests such as those in Figure 4.8 were omitted.

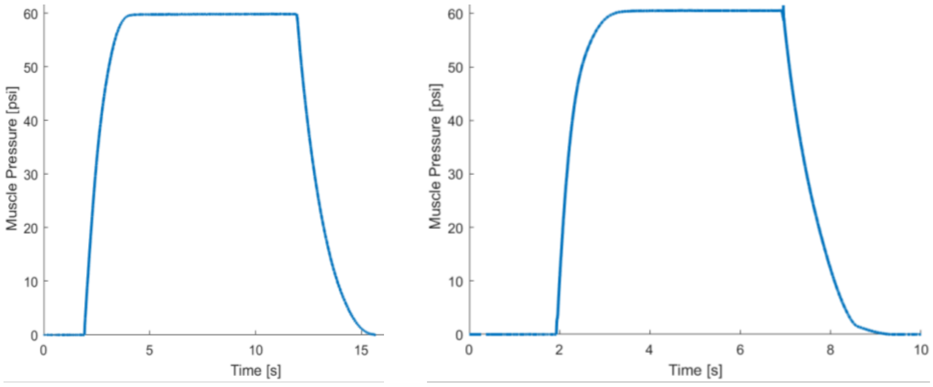

Figure 4.4 Muscle pressure step response for non-sleeved (LHS) and sleeved (RHS) muscle at 0% contraction and 60psi

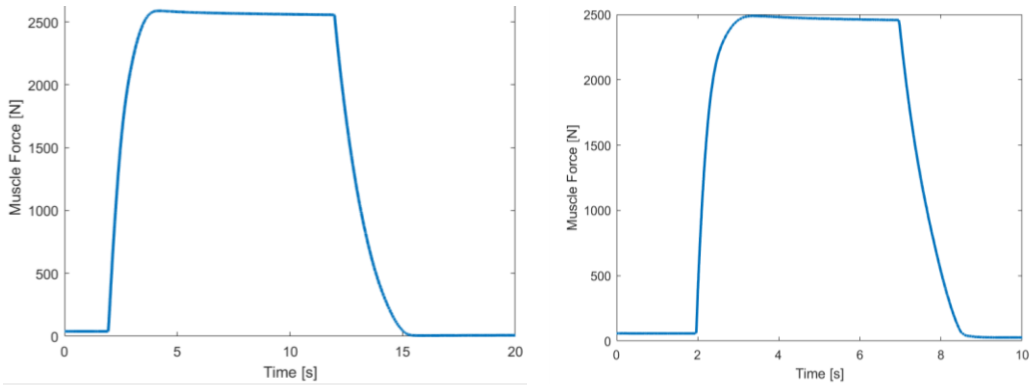

Figure 4.5 Muscle force response for non-sleeved (LHS) and sleeved (RHS) muscle at 0% contraction and 60psi

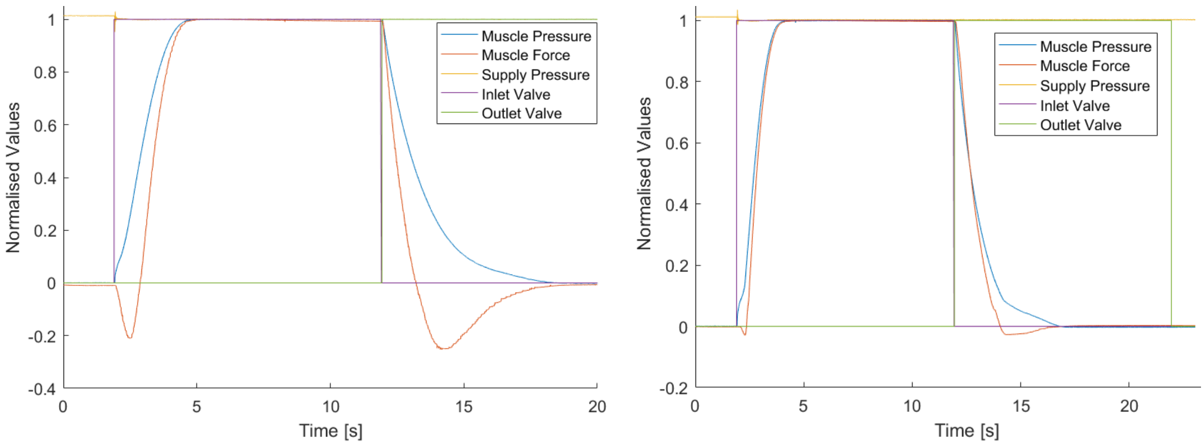

Figure 4.6 Normalised response variables for non-sleeved (LHS) and sleeved muscle (RHS) at 25% contraction and 60psi

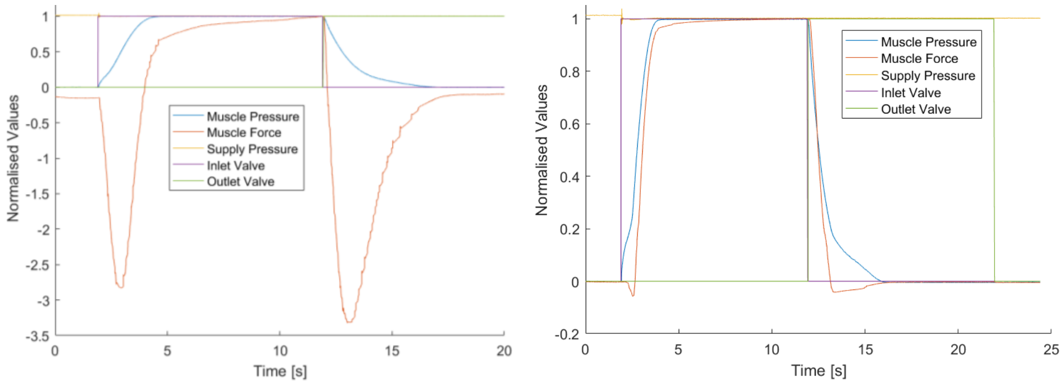

Figure 4.7 Normalised response variables for non-sleeved (LHS) and sleeved muscle (RHS) at 25% contraction and 30psi

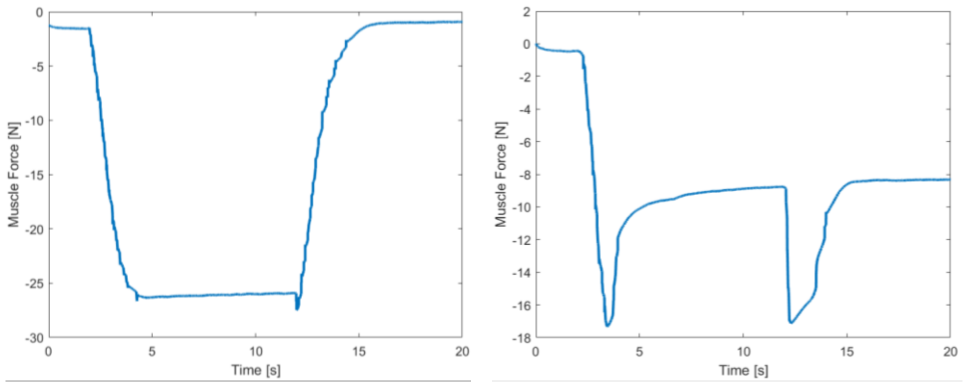

Figure 4.8 Muscle force response for non-sleeved (LHS) and sleeved (RHS) muscle at 25% contraction and 10psi

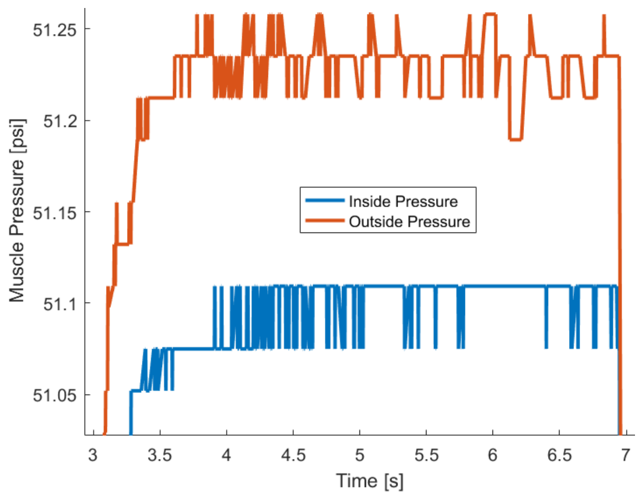

Figure 4.9 Close up of the pressure readings inside and outside the sleeved muscle at 0% contraction and 50psi

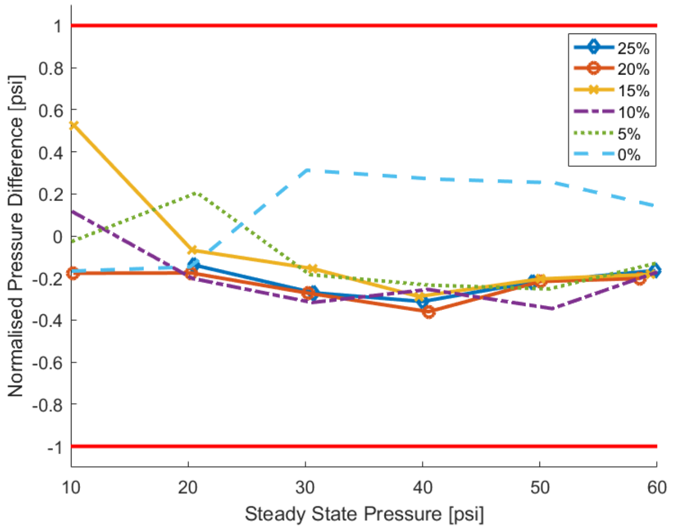

Figure 4.10 Normalised pressure difference at steady state for each contraction ratio

4.1.2 Rise Time Comparison

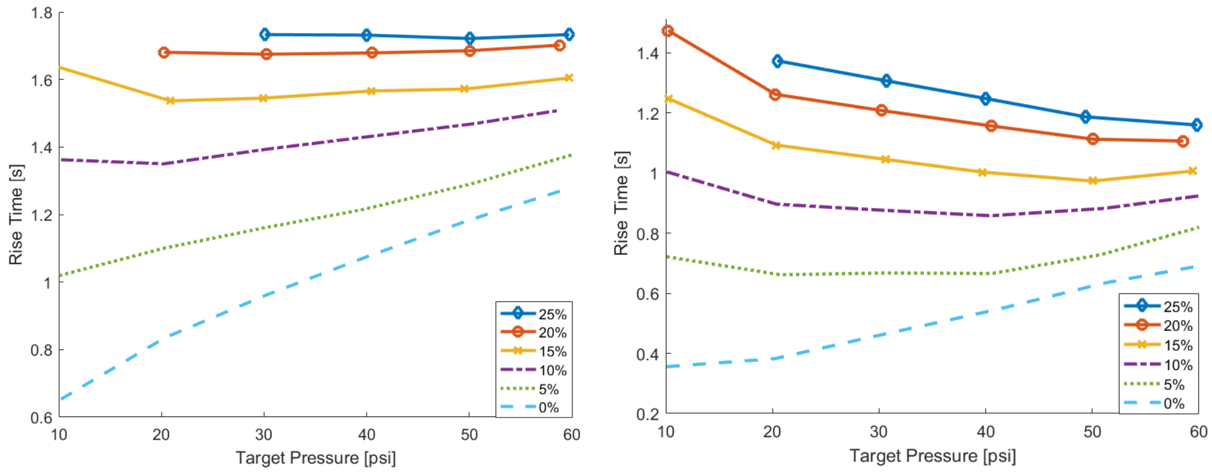

Figure 4.11 Rise time versus target pressure for non-sleeved (LHS) and sleeved (RHS) at varying contraction ratios

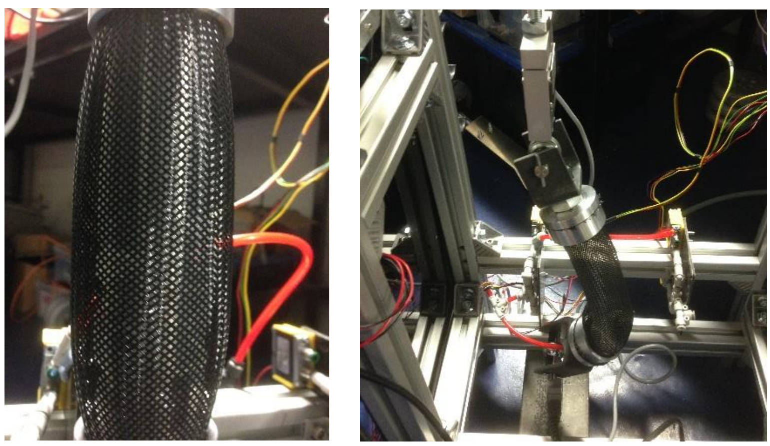

Figure 4.12 Significant crumpling of the internal bladder in the sleeved muscle (LHS) and the "buckling" of the non-sleeved muscle (RHS)

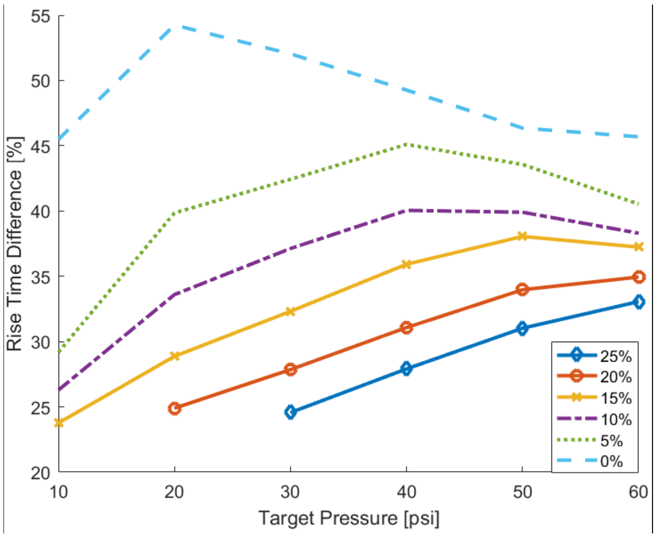

Figure 4.13 Percentage difference in rise time between the non-sleeved and sleeved muscles (from Figure 4.11) as a function of target pressure for varying contractions

The average difference in rise time across all pressures and all contraction ratios i.e. the average value of the blue curve in Figure 4.14, is calculated to be 36%. The orange and red curves in Figure 4.14 represent the maximum and minimum difference, respectively, in rise time encountered over the target pressure range for a particular contraction. The average of these curves is calculated to be 41% and 29%, again respectively.

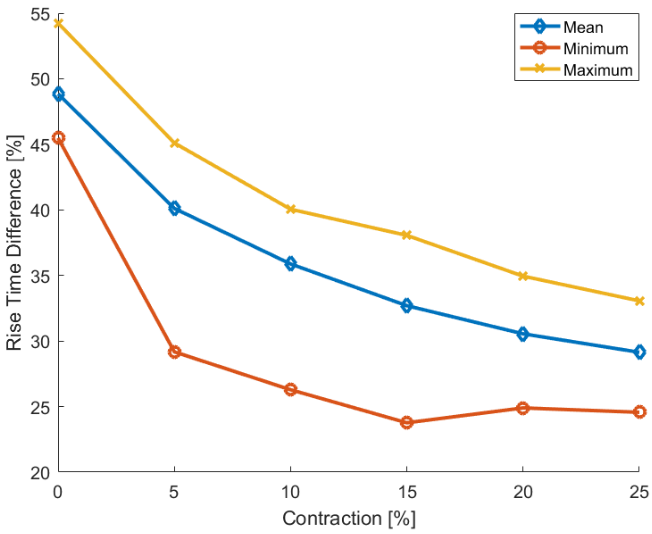

Figure 4.14 Percentage difference in rise time between non-sleeved and sleeved muscle averaged over the target pressure range for each level of contraction (blue)

4.2 Isotonic Step Response

4.2.1 Individual Step Response

The Isotonic step response of both muscles subject to 20-180N of applied loading was investigated over a 0-60psi pressure range. An example of the typical output from one of these tests for the non-sleeved and sleeved muscles are shown below in Figure 4.15 respectively.

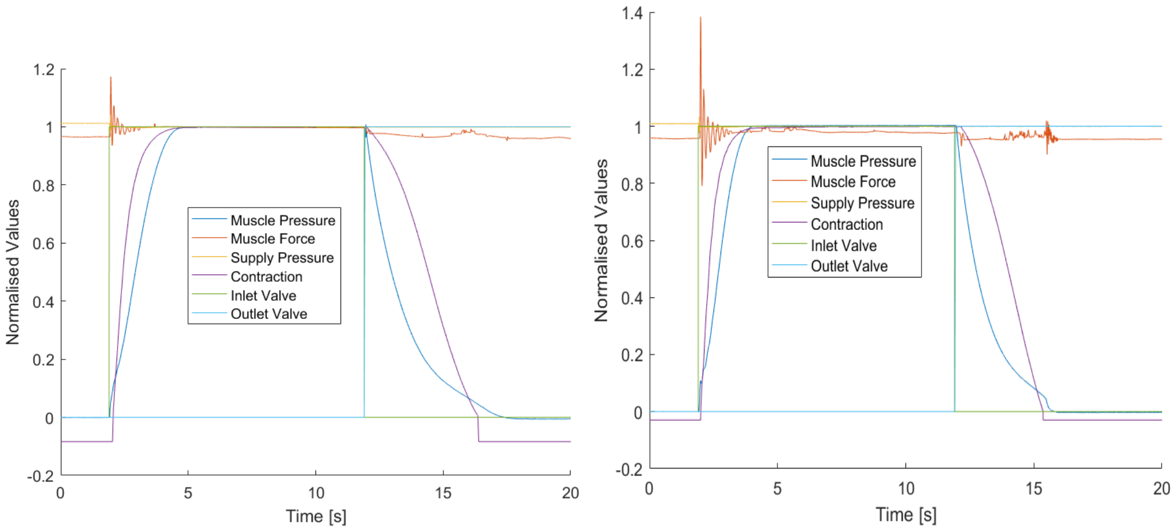

Figure 4.15 Normalised response variables for non-sleeved (LHS) and sleeved (RHS) at 60psi and 180N loading

Considering Figure 4.16, it is clear that there are significant dynamic forces on the muscle when the inlet valve is first opened and in the case of the sleeved muscle, these oscillations last for almost the entirety of the muscle's contraction (Figure 4.15). It is most likely that the greater muscle force generated by the greater $\frac{dV}{dL}$ of the sleeved muscle at initial contractions, is responsible for the greater magnitude and duration of these oscillations.

These oscillations do mean that the test is not truly isotonic, however as they occur at a frequency far higher than that of muscle contraction, they do not significantly affect the test. They are also present in both tests (albeit to a lesser severity in the non-sleeved muscle) so the comparison of isotonic rise time between the two muscles is still valid. The steady state force post oscillation is noticeably higher than the initial load and therefore it is the average of this steady state force that is quoted hereafter.

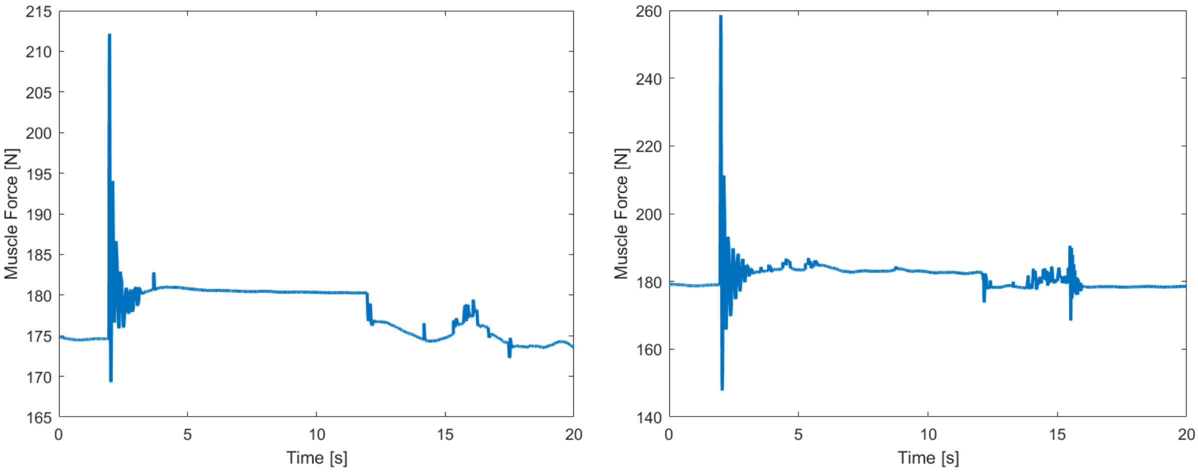

Figure 4.16 Muscle force response for non-sleeved (LHS) and sleeved (RHS) at 60psi and 180N loading

Although the pressure step response of both muscles under all loading and supply pressure combinations is smooth and would provide an adequate measure of response time, it was the contraction of the muscle that was instead used as the rise time criteria. The reason for this is due to the different extents of contractions of the two muscles under the same pressure input (the contraction of the sleeved muscle is always greater). Accordingly, a fairer stipulation of the rise time criteria at a certain supply pressure was the time taken to go from 10% to 90% of 75% of the steady-state non-sleeved contraction subject to full loading i.e. the minimum contraction achievable for that pressure at any weight. The 25% reduction in the rise time goal factors out the slowing down of the muscle as it approaches steady state, ensuring that for any weight and for both muscles, contraction is evaluated during the same fast-climb phase.

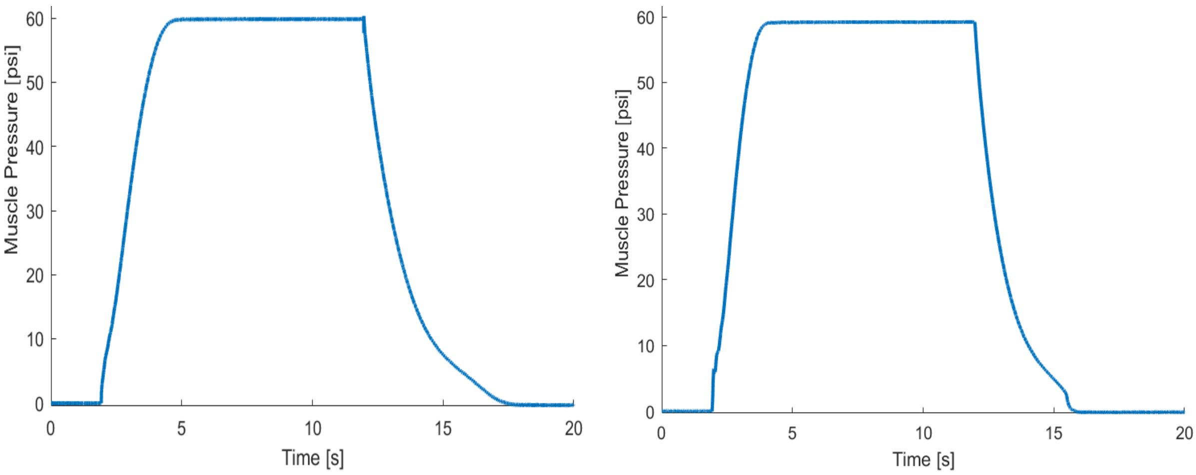

Figure 4.17 Muscle pressure response for non-sleeved (LHS) and sleeved (RHS) at 60psi and 180N loading

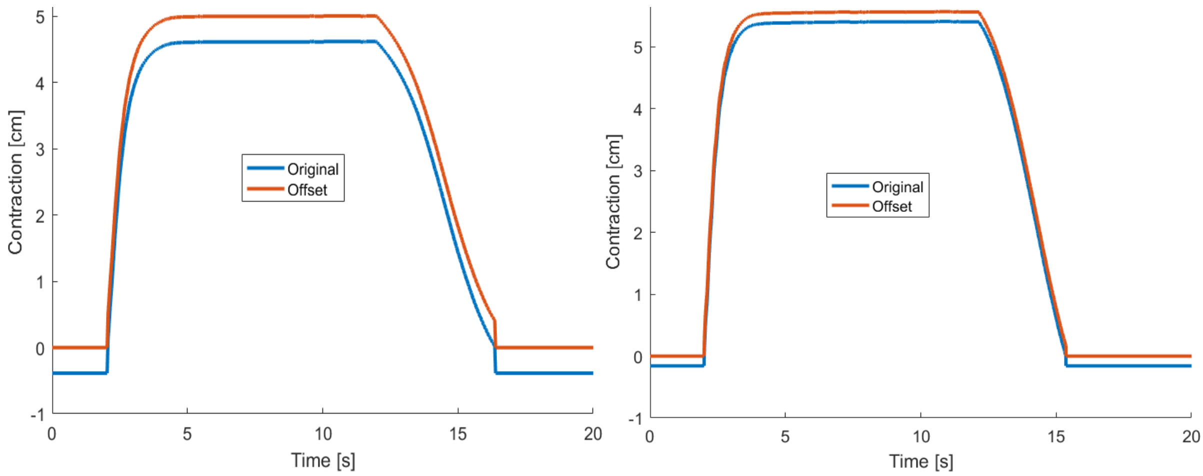

Figure 4.18 Muscle contraction response for non-sleeved (LHS) and sleeved (RHS) at 60psi and 181N loading

Before cycling through the different weights at a certain pressure, the encoder set point was reset at the rest position with the lowest weight applied. Consequently, when greater loads were applied to the pulley, there was a greater stretch in the muscles and the angle corresponding to the encoder's rest position was decreased (Figure 4.18 and Figure 4.19). The offsets applied to the contraction responses for weights above the initial weight (Figure 4.19), allowed for easier visual determination of a muscle's final contraction and simplified the determination of rise time.

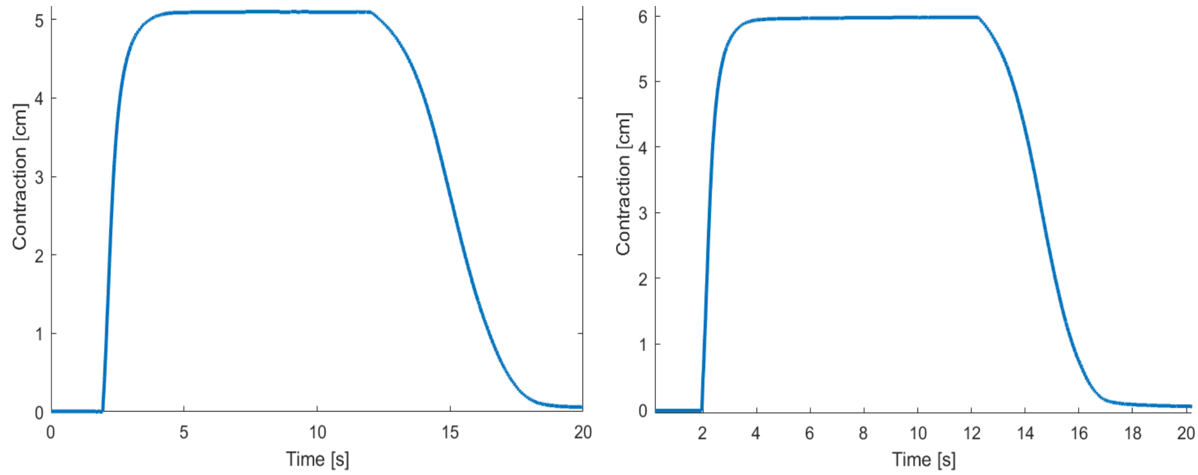

Figure 4.19 Muscle contraction response for non-sleeved (LHS) and sleeved (RHS) at 60psi and 24N loading

Similar to the Isometric tests, the fast recovery of the supply pressure ensures a steady pressure target for the duration of the muscle's transient response (Figure 4.15 and Figure 4.20).

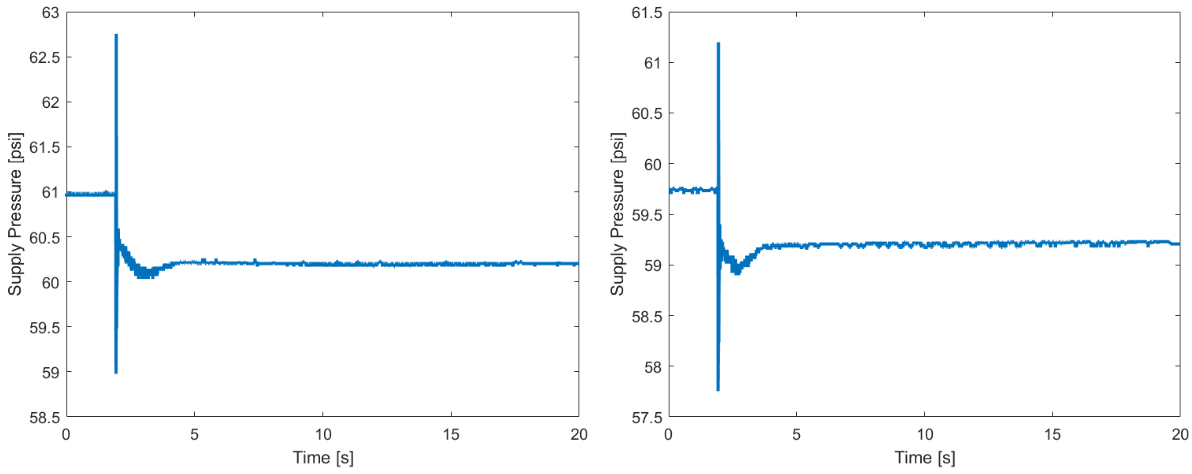

Figure 4.20 Supply Pressure response for non-sleeved (LHS) and sleeved (RHS) at 60psi and 180N loading

4.2.2 Rise Time Comparison

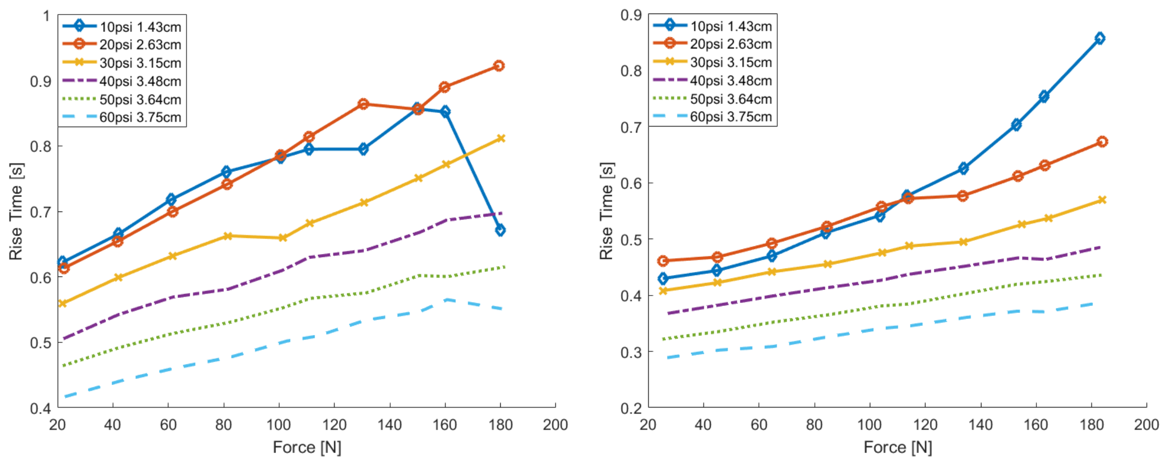

Figure 4.21 Rise time versus load at varying supply pressure for non-sleeved (LHS) and sleeved (RHS). The contraction target according to the definition provided in Section 4.2.1 is provided along with the corresponding pressure target in the legend attached to each figure.

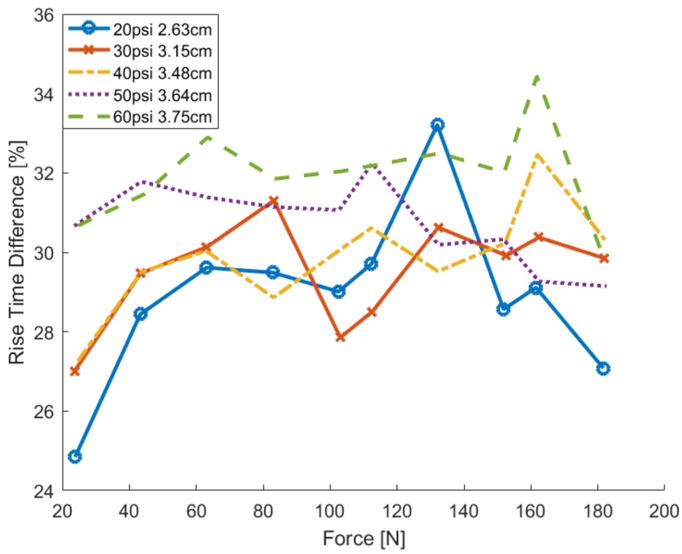

Figure 4.22 Difference in rise time between non-sleeved and sleeved versus load at varying supply pressure (10psi outlier omitted)

The mean rise time difference over all target pressure and loading levels i.e. the average value of the blue curve in Figure 4.23, is calculated to be 30%. The orange and red curves in Figure 4.23 represent the maximum and minimum difference, respectively, in rise time encountered over the target pressure range for a particular load. The average of these curves is calculated to be 32% and 28%, again respectively.

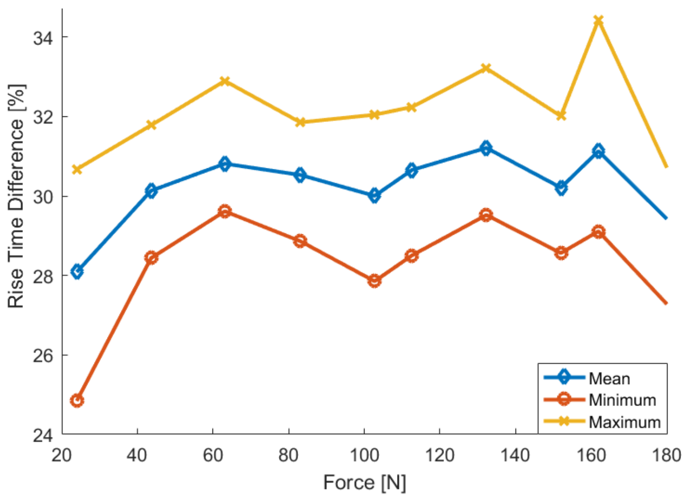

Figure 4.23 Percentage difference in rise time averaged over target pressure for each increment of loading (blue)

4.3 Antagonistic Step Response

This test involved the operation of two muscles arranged antagonistically to actuate an arm by means of a pulley. The response was recorded while pressure was alternated between supply pressure and ambient in alternate muscles when the arm reached a specified angle (e.g. +/-10°).

4.3.1 Individual Angle Step Response

Note that all subsequent figures in this Subsection 4.3.1 start at a time substantially after 0 seconds because this initial period was used to adjust the lever arm to the horizontal by changing the muscle pressures.

It is obvious from the left hand image of Figure 4.24 that the muscle stutters during contraction causing the lever arm to oscillate significantly as it is raised. This is symptomatic of the changing moment arm of the applied weight during contraction. The oscillation of the non-sleeved muscle is most pronounced on the rise to the horizontal point as the muscle has to rapidly increase force to overcome the increased torque.

Similarly, as the lever arm moves above the neutral angle, the moment arm decreases and the muscle force must now decrease. It is this variation in the force required of the upper contracting muscle, which causes it to bounce on the incline. On the way down, the motion of the applied load is governed more by the force of gravity and depends less on the force output of the muscles to control its motion, thereby producing a much smoother motion. As expected the fall time of the muscle is dramatically less than the rise time because the weight is falling with gravity.

On the other hand, the angular motion of the sleeved muscle is much smoother and there does not seem to be a significant difference in the rise and fall times of the muscle. The smoother motion of the sleeved muscle is due to the increased force output (Figure 4.25) easily overcoming the increasing torque requirement raising up to the zero point and then the increased rigidity from the central element reduces vibrations arising from the decreasing applied torque above the horizontal.

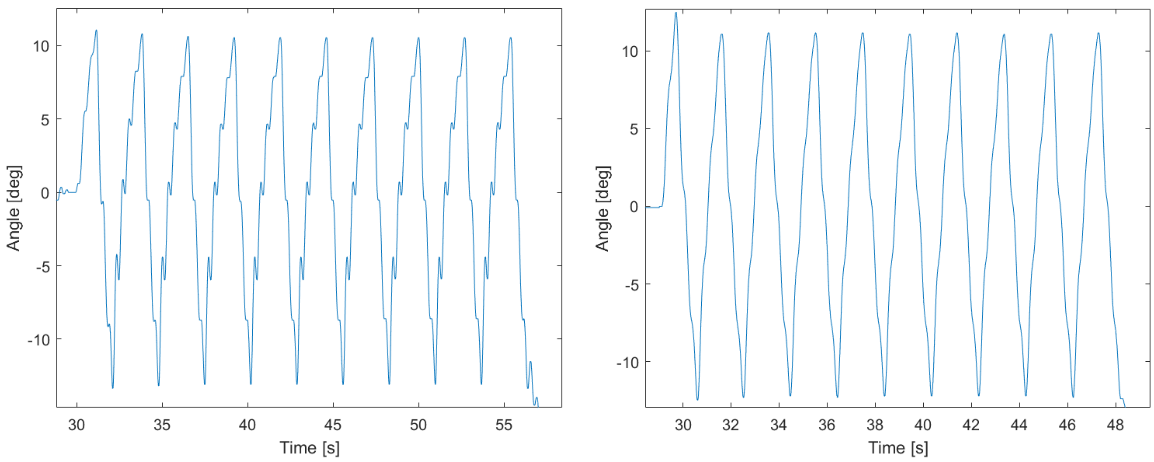

Figure 4.24 10^0 step response of non-sleeved (LHS) and sleeved (RHS) muscles at 60psi and 5kg

Due to the horizontal orientation of the antagonistic setup, the top muscle of the pair will always be subject to a much higher force because it has to counteract gravity (Figure 4.25). The oscillations in the force response are due once again to the varying joint torque but the force output of the sleeved muscle is more greatly affected. This could be an indication of the muscle's greater ability to react to the changing torque by constantly adjusting its own force output.

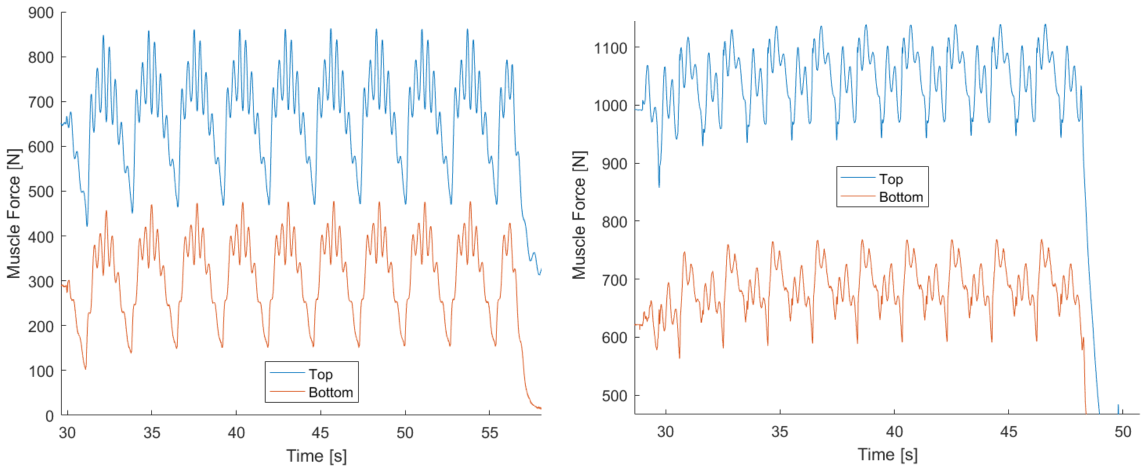

Figure 4.25 Force step response of non-sleeved (LHS) and sleeved (RHS) muscles at 60psi, 5kg, and 10^0 displacement

The pressure behaviour of both the top and bottom muscle is as expected, demonstrating the inverse relationship that is required to actuate the joint antagonistically (Figure 4.26 and Figure 4.27). The response of the supply pressure is much more interesting because it follows a jagged wave at double the frequency of the muscle pressure response because two valve openings occur for every one oscillation of the joint (Figure 4.28). The sudden opening of a muscle inlet valve causes a substantial drop in the supply pressure before the regulator takes effect, causing the supply pressure to rise even as one muscle is being filled. The delay between the inlet valve of one muscle closing and the inlet valve of the other opening gives the regulator enough of a window to re-establish the original supply pressure, producing the distinctive spikes evident in Figure 4.28.

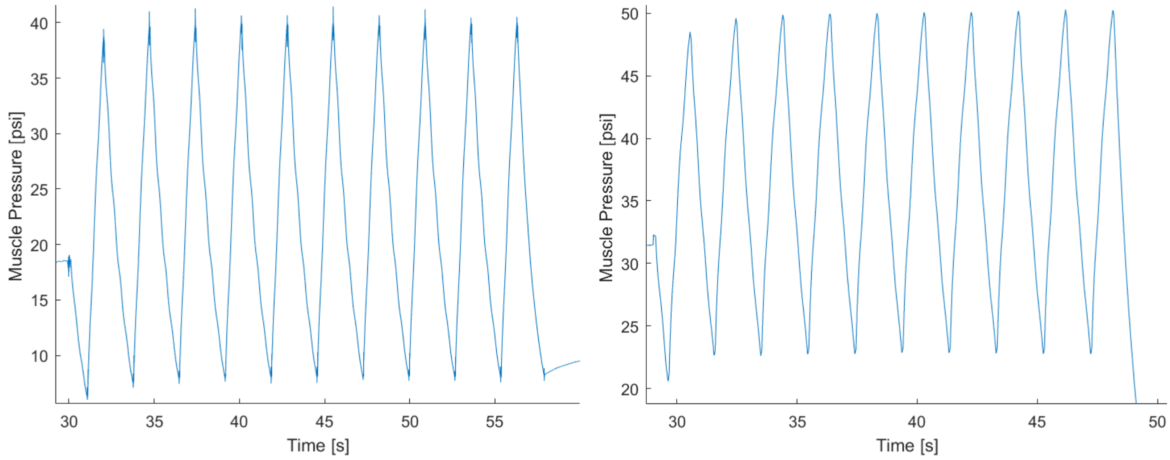

Figure 4.26 Pressure step response of non-sleeved (LHS) and sleeved (RHS) bottom muscle at 60psi, 5kg, and 10^0 displacement

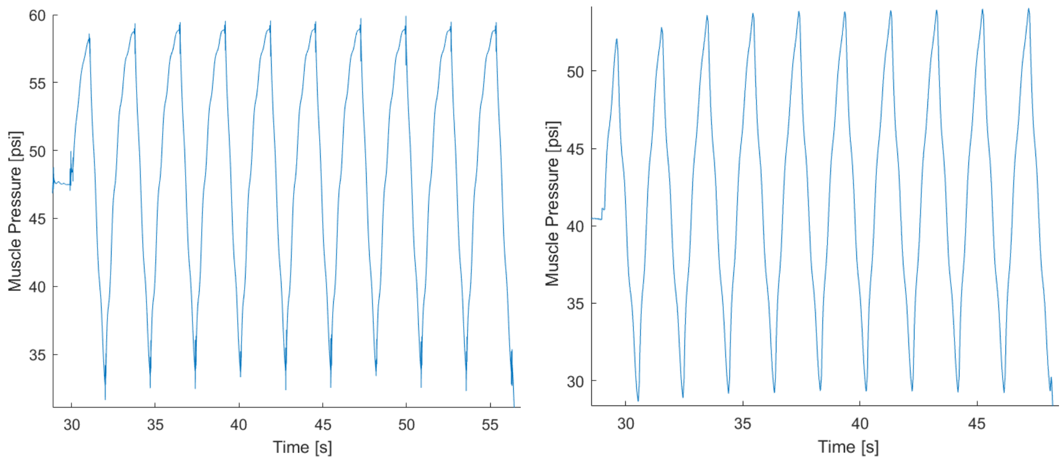

Figure 4.27 Pressure step response of non-sleeved (LHS) and sleeved (RHS) top muscle 60psi, 5kg, and 10^0 displacement

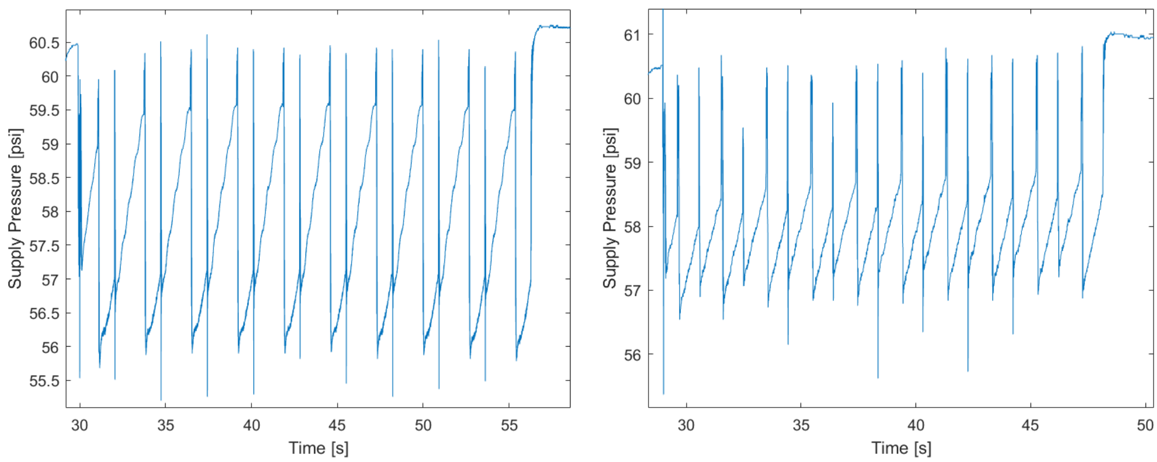

Figure 4.28 Supply pressure response of non-sleeved (LHS) and sleeved (RHS) muscles at 60psi, 5kg, and 10^0 displacement

4.3.2 Rise Time Comparison

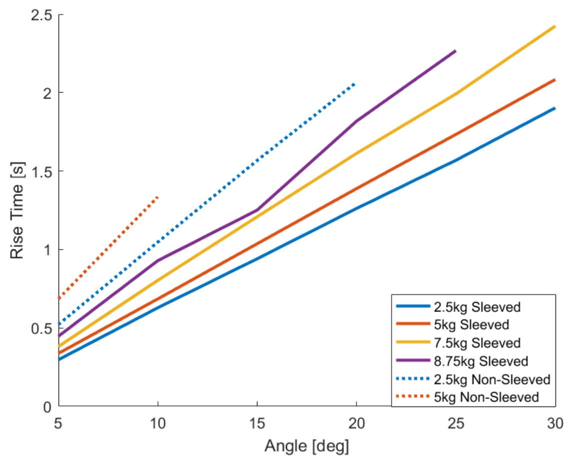

Figure 4.29 Rise time comparison between the sleeved and non-sleeved muscle as a function of angular displacement at different loading conditions

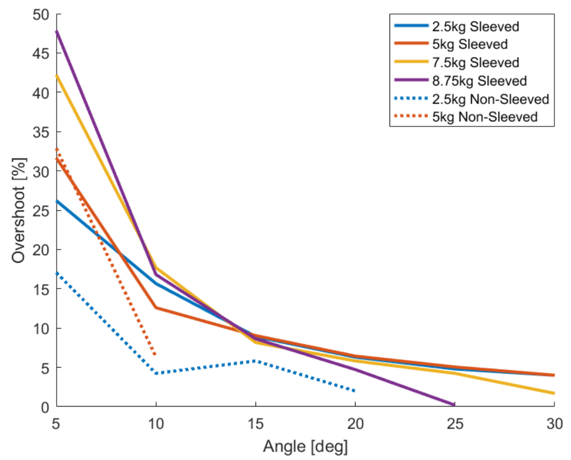

Figure 4.30 Percentage overshoot comparison between the sleeved and non-sleeved muscle as a function of angular displacement at different loading conditions

4.4 Antagonistic Disturbance Response

In the following tests the antagonistically actuated joint with applied load was offset from its set point manually, then released instantaneously. This simulates a typical disturbance such as when a load is dropped.

Once again the time axis of the three following figures is offset from zero because this initial period was used to adjust to the neutral point at the start of the test.

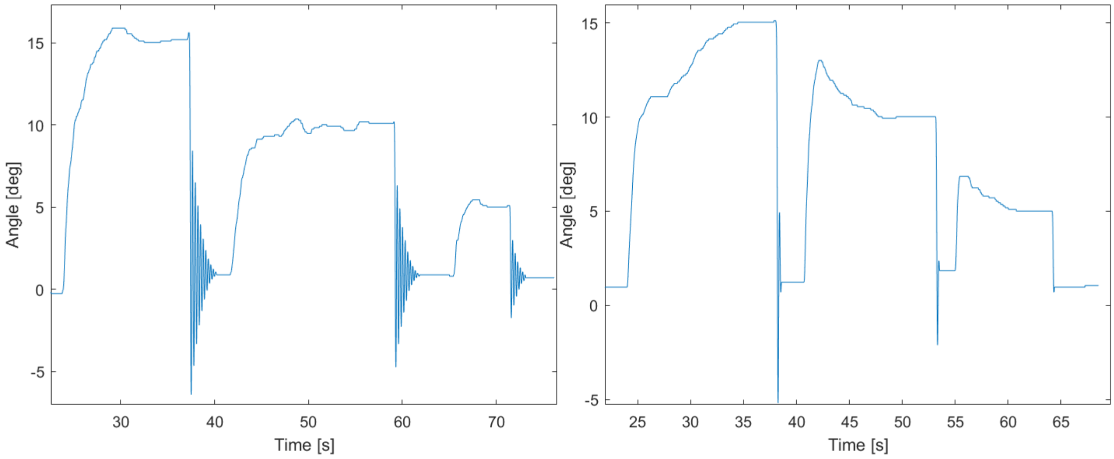

Figure 4.31 Response of the non-sleeved (LHS) and sleeved (RHS) antagonistic configuration to initial angular displacements of 5^0,10^0, and 15^0 at 2.5kg loading

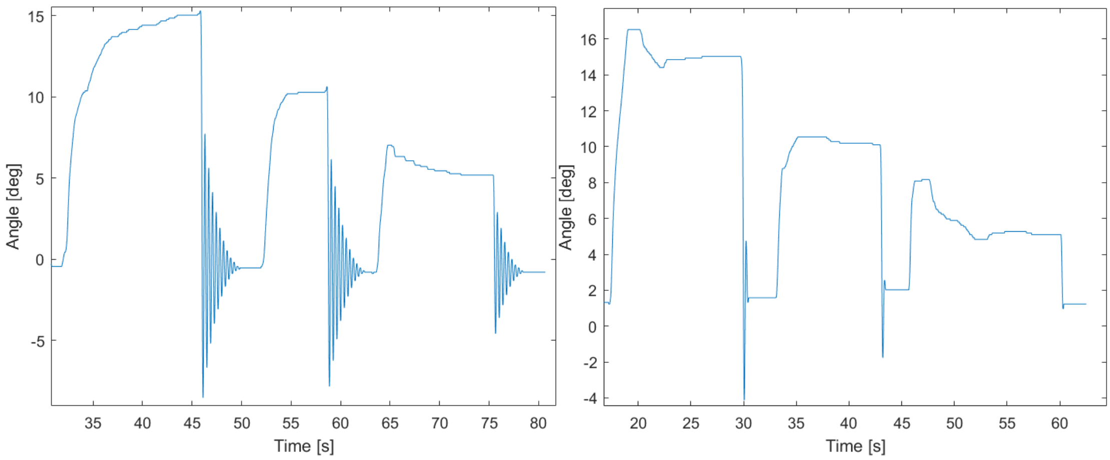

Figure 4.32 Response of the non-sleeved (LHS) and sleeved (RHS) antagonistic configuration to initial angular displacements of 5^0,10^0, and 15^0 at 5kg loading

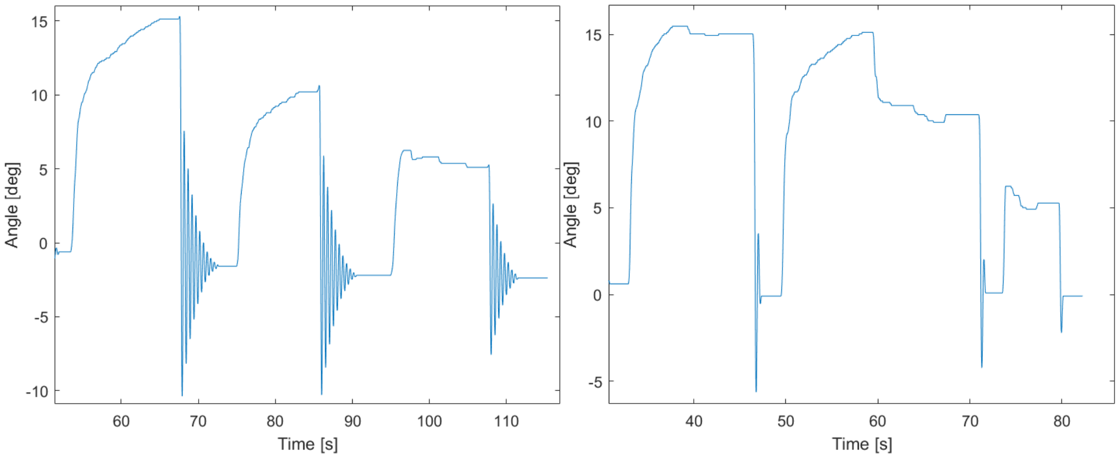

Figure 4.33 Response of the non-sleeved (LHS) and sleeved (RHS) antagonistic configuration to initial angular displacements of 5^0,10^0, and 15^0 at 7.5kg loading

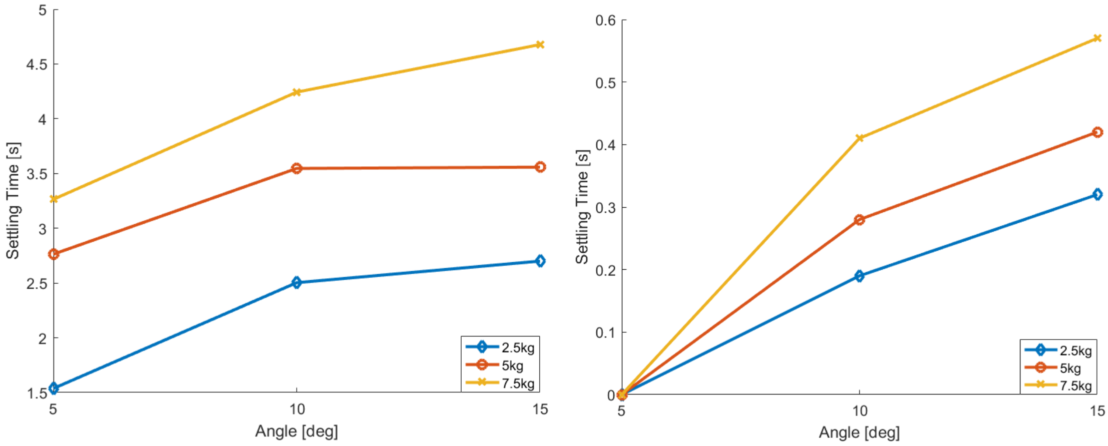

Figure 4.34 Settling time versus initial angular displacement for non-sleeved (LHS) and sleeved (RHS) muscle at varying loads

	10^0	15^0
2.5kg	92%	88%
5kg	92%	88%
7.5kg	90%	88%

Table 8 Percentage difference in settling time between non-sleeved and sleeved muscle at various load and angular displacement combinations

5 Discussion

5.1 Isometric and Isotonic Inflation Vs Deflation

A noticeable trend across all the single muscle tests for both the sleeved and non-sleeved muscles is that it takes significantly longer to deflate. This is the case even though the muscle is inflating and deflating from the same pressure range e.g. 0-60psi or 60-0psi as in Figure 4.4 and Figure 4.17. In an attempt to rationalise this behaviour the electrical analogy of one capacitor discharging through a resistor to another capacitor will be considered, similar to the approach of Chou and Hannaford [20]. The time constant for this process is given by,

$$\tau = \frac{RC_1C_2}{C_1 + C_2} \tag{12}$$

$$\tau_{inflation} = \frac{R_{inf}C_{muscle}}{\frac{C_{muscle}}{C_{tank}} + 1} \qquad \tau_{deflation} = \frac{R_{def}C_{muscle}}{\frac{C_{muscle}}{C_{room}} + 1}$$

where the volume of the muscle, tank, and room have been likened to capacitance and piping head losses have been likened to resistance.

Since both the capacitance of the room and tank are much greater than that of the muscle, the time constants for inflation and deflation both reach a limit equal to the product of muscle capacitance and their own resistance. However, since the volume of the room being exhausted to is greater than that of the tank, this will tend towards a larger time constant and slower deflation. On the other hand the greater length of piping and the greater number of push-fit connections between the supply and muscle compared to the muscle and the room would tend to a quicker deflation. Similarly, the deflation of the muscle under isotonic conditions should be much faster because the load is being lowered with gravity as opposed to being lifted against gravity during inflation.

Therefore, it can deduced from the larger deflation times that the effect of the volumes involved during inflation and deflation is much more significant than the head losses involved and the effect of gravity. Even though the above time constant equation was derived on the assumption of constant capacitance, which is not true in the case of the changing muscle volume, it is useful in conveying how the volumes involved during inflation and deflation have an effect on the rates of inflation and deflation.

5.2 Isometric Response Time

As was expected from the experiments of Davis et al. [10] and as was predicted by Cullinan et al. [17] the response time of the sleeved muscle is much faster (at least 24%) than the non-sleeved muscle, producing a maximum decrease of 54% (Figure 4.11 and Figure 4.13).

As the contraction ratio is increased the muscle volume also increases, meaning that larger volumes have to be pressurised at larger contractions. Hence the rise time increases with increasing contraction ratio (Figure 4.11). However, it is clear that the spacing between the high contraction ratios e.g. 20 and 25%, is much less than the spacing between the lower contraction ratios. This is because the muscle is close to maximum volume at these larger contractions and so the difference in volume and therefore rise time between successive contractions will be smaller. The larger contractile range of the sleeved muscle means that this effect is less noticeable between the 20 and 25% series compared to the non-sleeved muscle.

The lower contractions in Figure 4.11 are close to linear, while the higher contractions move progressively towards being horizontal. Approximating the air as an ideal gas and differentiating yields an expression for the rate of change of pressure in the muscle (Equation 13). It can be seen that at higher contraction ratios where the volume is already close to maximum, then the V_m term will remain roughly constant as the supply pressure is varied and the second term can be approximated as zero since $\dot{V}_m = 0$. Accordingly, the rate of change of pressure at higher contractions is roughly proportional to the mass flow rate, which is in turn dependent on the supply pressure. As a result, increasing the supply pressure increases the rate of change of pressure but the target pressure is also higher so a balancing act occurs.

$$\dot{P}_m = \frac{1}{V_m}\left(\gamma R T \dot{m}_m - \gamma P_m \dot{V}_m\right) \tag{13}$$

where P_m is muscle pressure, V_m is muscle volume, γ is the specific heat ratio of air, R is the universal gas constant, T is the air temperature, and $\dot{m}_m$ is the mass flow rate of air into/out of the muscle.

At low contractions the volume of the muscle will increase appreciably as the target pressure is raised. This means that not only will there be successively larger divisions by V_m but the second term (containing $\dot{V}_m$) is no longer negligible and will reduce the rate of change of pressure. These effects combined with the increasing target pressures are more significant than the increased flow rates at these higher target pressures, leading to an increase in response time. Again the increased contractile range of the sleeved muscle means that there is still appreciable volume change at the higher contraction ratios, hence why there is less flattening compared to the non-sleeved muscle.

At higher contractions, especially for the sleeved muscle, it is noticeable that the rise time to reach 10psi is the greatest, which defies the argument made previously. The reason for this anomaly is believed to be due to the large amount of crumpling of the internal bladder around the central element of the sleeved muscle (Figure 4.12), leading to greater rise times for low pressures which struggled to unfurl the bladder.

Alternatively, this discrepancy could also be related to the threshold pressure of silicone being close to 10psi, meaning the muscle volume doesn't start to expand until the muscle pressure has almost reached supply pressure. At this stage because the driving pressure differential is so low, the flow rate into the muscle is greatly reduced (as can be seen in the decline in rate of pressure increase in Figure 4.1 and Figure 4.2). Therefore, more of the muscle volume has to be filled at this slower flow rate than for tests with higher pressures where the threshold pressure is overcome while there is a relatively large flow rate.

Comparing the LHS and RHS of Figure 4.11 it is clear that the sleeved muscle is more greatly affected by crumpling. This could be because with the sleeved muscle the silicon bladder is forced to furl over itself in overlapping layers around the rigid element, presenting a substantial restriction to the flow. On the other hand with the non-sleeved muscle the silicon and braid are free to buckle sideways and therefore it is much easier for the incoming air to inflate the bladder (Figure 4.12).

The volume difference between the sleeved and non-sleeved muscle is greatest at lower contractions when the majority of the sleeved volume is occupied by the rigid element. This explains why the greatest percentage decrease in response time occurs at the lowest contractions (Figure 4.13). Similarly, the vertical spacing between the contraction series decreases with greater contractions because the percentage volume saving decreases.

5.3 Isotonic Response Time

Once again, the rise time of the sleeved muscle is much improved on that on the conventional muscle (Figure 4.21), achieving a minimum decrease in rise time of 25% and a maximum of 34% (Figure 4.22).

As expected the greater force acting against the contraction of the muscle results in longer rise times (Figure 4.21). The previous relation (Equation 1) of Chou and Hannaford [20] can explain this intuitive behaviour. Equation 1 is restated below for convenience.

$$F = -P_m \frac{dV}{dL}$$

For a constant supply pressure, the muscle pressure will always traverse through the same range e.g. $0 \rightarrow P_{supply}$, during inflation. Remembering the isotonic nature of each test, it becomes apparent that in order to maintain contraction force through this $0 \rightarrow P_{supply}$ range for increasing applied load, the rate of change of volume with length will have to be greater at each stage of the muscle's inflation. For example, for a supply pressure of 60Pa, a starting muscle pressure of 10Pa, the range of change in volume with length will be greater for 180N compared to 60N,

$$\frac{dV}{dL} = \frac{60}{10 \rightarrow 60} = 6 \rightarrow 1 \quad or \quad \frac{dV}{dL} = \frac{180}{10 \rightarrow 60} = 18 \rightarrow 3$$

Since $\frac{dV}{dL}$ is greater, in order for the muscle to contract by a given amount dL, more air needs to be supplied to pressurise the greater associated increase in volume at higher loads compared to lower ones. Accordingly, it takes longer for the muscle to contract at higher loads.

Similarly, decreasing the supply pressure at constant loading reduces the muscle pressure range meaning that the $\frac{dV}{dL}$ range will be increased to compensate and the contraction rise time will be decreased once more.

The smaller internal volume of the sleeved muscle means that for any applied load and any muscle pressure range it will be able to provide the required $\frac{dV}{dL}$ range using less air and at a faster rate compared to the non-sleeved muscle (Figure 4.22).

5.4 Antagonistic Response Time

Out of all the figures in this report, Figure 4.29 is the one that best captures every aspect of the superior sleeved muscle performance. The first point of note from the figure is that there are only two series for the non-sleeved muscle, both of which are incomplete. This is because the non-sleeved muscle did not have the necessary force and contraction required to bring the lever arm to the positive angle setpoint (negative setpoint was not a problem because the muscle was aided by gravity).

Conversely, the increased contractile range and force output of the sleeved muscle were able to bring the lever arm through an angular range of 50^0 with almost 9kg of load when the non-sleeved muscle could only manage a range of 20^0 at 5kg. Furthermore, the response time of the sleeved muscle at this highest load is significantly faster than that of the non-sleeved muscle at the lightest load.

Considering Figure 4.30, it becomes clear that the ability of the sleeved muscle to rise quicker and with increased force/acceleration leads to greater overshoot than the non-sleeved muscle for the 2.5kg and 5kg cases. The sample size for this overshoot comparison is small, particularly for the 5kg case which only features two comparison points. Similarly, the fact that the trend is not as clear cut as in Figure 4.29 means that this is not a conclusive finding.

5.5 Antagonistic Disturbance Response

Comparison of the sleeved and non-sleeved performance at each of the three loading levels (Figure 4.31 to Figure 4.33) reveals the drastic difference in the ability of the two muscle types to reject disturbances. The sleeved muscle recovers almost immediately, undergoing a single oscillation at most for any disturbance and weight combination before reaching steady state. Conversely, the non-sleeved antagonistic set-up oscillates numerous times with larger magnitudes producing settling times that are at least 10 times and 8 times longer for the 10^0 and 15^0 disturbances respectively (Figure 4.34 and Table 8).

The rigid central element and reduced internal volume of air will manifest as greater stiffness which when combined with the greater inertia of the heavier SPAM explains the reduced magnitude of oscillation. Similarly, the continuous frictional force generated between the sliding seal and internal element of the SPAM will increase energy dissipation and contribute towards the reduced settling time.

5.6 Pressure Sensor Integration

As expected the positioning of the pressure sensor inside the muscle volume did not yield readings that were significantly different to those outside the muscle (Figure 4.9). The normalised pressure difference at each steady state pressure (SSP) (10-60psi) for each level of contraction is shown in Figure 4.10. The pressure difference between the two sensors was evaluated at steady state because this was the largest pressure reached for a particular test and would have produced the largest pressure difference between the two sensors. The Honeywell digital pressure sensors used in the experiment have a 12 bit resolution, which when spread over the 0-150psi range yields a value of 0.0366psi. This larger pressure difference at steady state gives the pressure sensors the best possible chance of detecting a difference in pressure between the two locations.

The accuracy of the Honeywell pressure sensors is quoted as 1% over the 1-150psi range, which is why each pressure difference at a particular SSP was normalised by 1% of that SSP. Since the difference curves for each contraction are within the +/- 1 error bounds over the entire SSP range, it can be concluded that there is no significant difference in pressure between these two locations. However, elsewhere in this report when a single value is quoted for the sleeved muscle pressure, it is that from the internal sensor because it should be the most accurate.

6 Conclusion

The inclusion of the central element into the conventional McKibben muscle design has imbued the SPAM with far superior static and now, dynamic performance in both the single and antagonistic setup.

Although, there was no significant difference between the pressure readings obtained from the sensors located inside and outside the sleeved muscle, the isometric tests proved that it is possible to incorporate a functioning pressure sensor inside the sleeved muscle volume. Integration of the sensor within the central element is a distinct advantage as it allows for a much more compact design and reduces ancillary hardware requirements e.g. the push-fit connection to split the output of the valve between the muscle and pressure sensor.

When researchers are predicting the bandwidth of a PAM and its supporting hardware i.e. the operating frequency above which the output of the PAM will become attenuated, the rise time of an output step response is commonly used in the calculation [20,21,35]. However, the isometric and isotonic single muscle tests of this research highlighted that it is actually the time taken for the muscle to deflate, which is the limiting factor on this system design. Consequently, the fall times for this set of experiments needs to be calculated and used to direct the search for methods of decreasing the deflation time such as larger orifice diameter valves for deflation.

Other results of the isometric tests revealed that the SPAM produced the greatest reductions in response time at low contractions where its decreased volume was most prominent. The average difference in response time over any contraction and any pressure was determined to be 36% and this difference never dropped below 24%. Similarly, a minimum reduction in response time of 25% and an average of 30% can be expected of the sleeved muscle when actuated under constant load.

The SPAM antagonistic configuration could not only lift heavier loads but it could do so faster than the conventional muscle lifting the lowest load through the same excursion. Additionally, the SPAM antagonistic configuration was able to move through a 60^0 excursion for all but the 8.75kg load and produced a much smoother motion while doing so. The recovery of the SPAM after a disturbance was also much better, producing one oscillation at most for 5^0,10^0, and 15^0 initial displacements. Conversely, the conventional muscle produced numerous oscillations which were of much larger magnitude and took at least 8 times longer to decay.

This improved robustness combined with smoother motion make the sleeved muscle much easier to control and hence more suited to robotics applications. However, the enhanced strength and faster inflation of the SPAM did lead to dramatic overshoot. Consequently, future work will involve developing a closed loop control algorithm to reduce this overshoot to an acceptable level.

The enhanced contractile range and response times of the SPAM address the main limitations of the traditional McKibben muscle, namely reduced actuation range and low bandwidth. This does come at the cost of incorporating a heavy, rigid element into the centre of the design, reducing the merit of the SPAM as a lightweight actuator. The way forward with SPAM design is therefore to seek to minimise the mass of the structural member while maintaining (or even improving) strength and internal volume occupation.

References

[1] Discover Magazine, 2008, “When Robots Live Among Us” [Online]. Available: http://cs.uvm.edu/~jbongard/Press/2008_5_27_Discover.pdf. [Accessed: 27-Jan-2017].

[2] Google, “A new way forward for mobility – Waymo” [Online]. Available: https://www.google.com/selfdrivingcar/. [Accessed: 27-Jan-2017].

[3] iRobot, “Roomba Robot Vacuum” [Online]. Available: https://www.irobot.com/For-the-Home/Vacuuming/Roomba.aspx. [Accessed: 27-Jan-2017].

[4] DARPA, “Debut of Atlas Robot” [Online]. Available: http://www.darpa.mil/about-us/timeline/debut-atlas-robot. [Accessed: 27-Jan-2017].

[5] Klute, G. K., and Hannaford, B., 1998, “Fatigue Characteristics of McKibben Artificial Muscle Actuators,” IEEE/RSJ International Conference on Intelligent Robots and Systems.

[6] Ham, R. Van, Daerden, F., and Lefeber, D., 2003, “Pressure Control with On-Off Valves of Pleated Pneumatic Artificial Muscles in a Modular One-Dimensional Rotational Joint .,” International Conference on Humanoid Robots.

[7] More, M., and Líška, O., 2013, “Comparison of different methods for pneumatic artificial muscle control,” IEEE 11th International Symposium on Applied Machine Intelligence and Informatics (SAMI), pp. 117–120.

[8] Reynolds, D. B., Repperger, D. W., Phillips, C. A., and Bandry, G., 2003, “Modeling the Dynamic Characteristics of Pneumatic Muscle,” Ann. Biomed. Eng., **31**(3), pp. 310–317.

[9] Tondu, B., 2012, “Modelling of the McKibben artificial muscle : A review,” J. Intell. Mater. Syst. Struct., **23**(3), pp. 225–253.

[10] Davis, S., Tsagarakis, N., Canderle, J., and Caldwell, D. G., 2003, “Enhanced Modelling and Performance in Braided Pneumatic Muscle Actuators,” Int. J. Rob. Res., **22**(3–4), pp. 213–227.

[11] Davis, S., and Caldwell, D. G., 2006, “pneumatic muscle actuators for humanoid applications - sensor and valve integration,” 6th IEEE-RAS International Conference on Humanoid Robots, pp. 456–461.

[12] Colbrunn, R. W., Nelson, G. M., and Quinn, R. D., 2001, “Modeling of braided pneumatic actuators for robotic control,” IEEE/RSJ International Conference on Intelligent Robots and Systems, pp. 1964–1970.

[13] Caldwell, D. G., Medrano-Cerda, G. A., and Goodwin, M., 1995, “Control of Pneumatic Muscle Actuators,” IEEE Control Syst. Mag., p. 40–48.

[14] Daerden, F., and Lefeber, D., 2002, “Pneumatic Artificial Muscles : actuators for robotics and automation,” Eur. J. Mech. Environ. Eng., **47**(1), pp. 11–21.

[15] Lilly, J. H., and Berlin, J. E., 2003, “Fuzzy PD+I Learning Control for a Pneumatic Muscle,” 12th IEEE Int. Conf. Fuzzy Syst., **1**, pp. 278–283.

[16] Vo-Minh, T., Tjahjowidodo, T., Ramon, H., and Van Brussel, H., 2011, “A new approach to modeling hysteresis in a pneumatic artificial muscle using the Maxwell-slip model,” IEEE/ASME Trans. Mechatronics, **16**(1), pp. 177–186.

[17] Cullinan, M. F., Bourke, E., Kelly, K., and Mcginn, C., 2016, “A McKibben Type Sleeve Pneumatic Muscle and Integrated Mechanism for Improved Stroke Length,” Int. J. Mech. Robot.

[18] Kingsley, D. A., and Quinn, R. D., 2002, “Fatigue life and frequency response of braided pneumatic actuators,” IEEE Int. Conf. Robot. Autom., **3**, pp. 2830–2835.

[19] Mortier, K., 2014, “Braided pneumatic muscles for rehabilitation apparatus Karsten Mortier.”

[20] Chou, C., and Hannaford, B., 1996, “Measurement and modeling of McKibben pneumatic artificial muscles.,” IEEE Trans. Robot. Autom., **12**(1), pp. 90–102.

[21] Shen, X., 2010, “Nonlinear model-based control of pneumatic artificial muscle servo systems.,” Control Eng. Pract., **18**(3), pp. 311–317.

[22] Jouppila, V. T., Gadsden, S. A., Bone, G. M., Ellman, A. U., and Habibi, S. R., 2014, “Sliding mode control of a pneumatic muscle actuator system with a PWM strategy.,” Int. J. Fluid Power, **15**(1), pp. 19–31.

[23] Vanderborght, B., 2007, “Dynamic stabilisation of the biped Lucy powered by actuators with controllable stiffness.”

[24] Vocke III, R. D., Kothera, C. S., and Wereley, N. M., 2014, “Mechanism and bias considerations for design of a bi-directional pneumatic artificial muscle actuator.,” Smart Mater. Struct., **23**(12).

[25] Murillo, J., 2013, “Design of a Pneumatic Artificial Muscle For Powered Lower Limb Prostheses.”

[26] Doumit, M. D., 2009, “Characterization, modeling and design of the braided pneumatic muscle.”

[27] D.W.Repperger, 1999, “Controller Design Involving Gain Scheduling for a Large Scale Pneumatic Muscle Actuator.,” IEEE Int. Conf. Control Appl., **1**, pp. 285–290.

[28] Caldwell, D. G., and Goodwin, M. J., 1993, “Braided Pneumatic Actuator Control of a Multi-Jointed Manipulator.,” IEEE International Conference on Systems, Man and Cybernetics: Systems Engineering in the Service of Humans., IEEE, pp. 423–428.

[29] Colbrunn, R. W., Nelson, G. M., and Quinn, R. D., 2001, “Design and control of a robotic leg with braided pneumatic actuators.,” IEEE/RSJ International Conference on Intelligent Robots and Systems: Expanding the Societal Role of Robotics in the the Next Millennium, pp. 992–998.

[30] Medrano-Cerda, G. A., Bowler, C. J., and Caldwell, D. G., 1995, “Adaptive Position Control of Antagonistic Pneumatic Muscle Actuators.,” IEEE/RSJ International Conference on Intelligent Robots and Systems 95.’Human Robot Interaction and Cooperative Robots’, pp. 378–383.

[31] Quinn, R. D., Nelson, G. M., Bachmann, R. J., Kingsley, D. A., Offi, J. T., Allen, T. J., and Ritzmann, R. E., 2003, “Parallel Complementary Strategies for Implementing Biological Principles into Mobile Robots,” Int. J. Rob. Res., **22**(3–4), pp. 169–186.

[32] van der Linde, R. Q., 1999, “Design, analysis, and control of a low power joint for walking robots, by phasic activation of McKibben muscles,” IEEE Trans. Robot. Autom., **15**(4), pp. 599–604.

[33] van der Smagt, P., Groen, F., and Schulten, K., 1996, “Analysis and control of a rubbertuator arm,” Biol. Cybern., **75**(5), pp. 433–440.

[34] Diep, T. U., Thanh, C., and Ahn, K. K., 2006, “Nonlinear PID control to improve the control performance of 2 axes pneumatic artificial muscle manipulator using neural network,” Mechatronics, **16**(9), pp. 577–587.

[35] Shin, D., Sardellitti, I., and Oussama, Y. P., 2010, “Design and Control of a Bio-Inspired Human-Friendly Robot,” Int. J. Rob. Res., **29**(5), pp. 571–584.

[36] Tondu, B., and Lopez, P., 2000, “Modeling and Control of McKibben Artificial Muscle

Actuators.,” IEEE Control Syst., **20**(2), pp. 15–38.
[37] Tondu, B., 2013, “Closed-Loop Position Control of Artificial Muscles with a Single Integral Action: Application to robust positioning of McKibben artificial muscle,” IEEE International Conference on Mechatronics, pp. 718–723.
[38] Carbonell, P., Jiang, Z. P., and Repperger, D. W., 2001, “Nonlinear control of a pneumatic muscle actuator: backstepping vs. sliding-mode,” Proc. IEEE Int. Conf. Control Appl., **2**, pp. 167–172.
[39] Lilly, J. H., and Yang, L., 2005, “Sliding mode tracking for pneumatic muscle actuators in opposing pair configuration,” IEEE Trans. Control Syst. Technol., **13**(4), pp. 550–558.
[40] Cai, D., and Dai, Y., 2000, “A sliding mode controller for manipulator driven by artificial muscle actuator,” International Conference on Control Applications, pp. 668–673.
[41] Van Damme, M., Vanderborght, B., Van Ham, R., Verreist, B., Daerden, F., and Lefeber, D., 2007, “Proxy-based sliding mode control of a manipulator actuated by pleated pneumatic artificial muscles,” IEEE International Conference on Robotics and Automation, pp. 4355–4360.
[42] Zhang, L., Xie, J., and Lu, D., 2007, “Adaptive robust control of one-link joint actuated by pneumatic artificial muscles,” 1st International Conference on Bioinformatics and Biomedical Engineering, ICBBE, pp. 1185–1189.
[43] Zhu, X., Tao, G., Yao, B., and Cao, J., 2008, “Adaptive robust posture control of a parallel manipulator driven by pneumatic muscles,” Automatica, **44**(9), pp. 2248–2257.
[44] Balasubramanian, K., and Rattan, K. S., 2003, “Feedforward control of a non-linear pneumatic muscle system using fuzzy logic,” 12th IEEE Int. Conf. Fuzzy Syst., **1**, pp. 272–277.
[45] Petrovic, P. B., 2002, “Modeling and control of an artificial muscle part one: Model building,” Conf. Mechan. Vibrations, pp. 93–98.
[46] Tian, S., Ding, G., Yan, D., Lin, L., and Shi, M., 2004, “Nonlinear Controlling of Artificial Muscle System with Neural Networks,” IEEE Int. Conf. Robot. Biomimetics, pp. 56–59.
[47] Jamwal, P. K., and Xie, S. Q., 2012, “Artificial Neural Network Based Dynamic Modelling of Indigenous Pneumatic Muscle Actuators,” IEEE/ASME International Conference on Mechatronics and Embedded Systems and Applications (MESA), pp. 190–195.
[48] Driver, T., and Shen, X., 2013, “Sleeve Muscle Actuator: Concept and Prototype Demonstration,” J. Bionic Eng., **10**(2), pp. 222–230.
[49] Shin, D., Sardellitti, I., and Khatib, O., 2008, “A Hybrid Actuation Approach for Human-Friendly Robot Design,” IEEE International Conference on Robotics and Automation, pp. 1747–1752.
[50] Festo, “DMSP/MAS Fluidic Muscle” [Online]. Available: https://www.festo.com/rep/en_corp/assets/pdf/info_501_en.pdf. [Accessed: 27-Jan-2017].
[51] Matrix, “Solenoid Valves 820 Series” [Online]. Available: http://www.bibus.hu/fileadmin/editors/countries/bihun/product_data/matrix/documents/matrix_series_820_2-2_3-3_solenoid_valves_catalogue_en.pdf. [Accessed: 27-Jan-2017].
[52] KV Automation Systems, “FAS 15 mm MICROSOL Direct acting solenoid valve”

[Online]. Available: http://fas.ch/pdf/X0120009.pdf. [Accessed: 27-Jan-2017].
[53] Joucomatic, “Proportional Mini Piezo-Valves Piezotronic” [Online]. Available: http://www.valves-direct.com/media/specs/Series_630_-_ASCO_JOUCOMATIC_Piezotronic.pdf. [Accessed: 27-Jan-2017].
[54] Matrix, “Solenoid Valves 750 Multi-Function Series” [Online]. Available: http://www.bibus.hu/fileadmin/editors/countries/bihun/product_data/matrix/documents/matrix_series_750_2-2_3-2_multi_functional_catalogue_en.pdf. [Accessed: 27-Jan-2017].
[55] Festo, “MPPE/MPPES Proportional Pressure Regulators” [Online]. Available: https://www.festo.com/cat/en-gb_gb/data/doc_ENUS/PDF/US/MPPE-MPPES_ENUS.PDF. [Accessed: 27-Jan-2017].
[56] Festo, “MPYE Proportional Directional Control Valves” [Online]. Available: https://www.festo.com/cat/en-gb_gb/data/doc_ENGB/PDF/EN/MPYE_EN.PDF. [Accessed: 27-Jan-2017].
[57] Festo, “MPP Proportional Pressure Regulators” [Online]. Available: https://www.festo.com/net/SupportPortal/Files/44239/MPP-3.pdf. [Accessed: 27-Jan-2017].
[58] Weiss, L. E., Merz, R., Prinz, F. B., Neplotnik, G., Padmanabhan, P., Schultz, L., and Ramaswami, K., 1997, “Shape deposition manufacturing of heterogeneous structures,” J. Manuf. Syst., **16**(4), pp. 239–248.
[59] Tsagarakis, N., Caldwell, D. G., and Medrano-Cerda, G. A., “A 7 DOF pneumatic muscle actuator (pMA) powered exoskeleton,” 8th IEEE International Workshop on Robot and Human Interaction, pp. 327–333.
[60] Davis, S., Tresadern, P., Canderle, J., Tsagarakis, N. G., Dodd, P., and Caldwell, D. G., 2003, “The biomimetic design of ‘soft’mechatronic systems,” 11th International Conference on Advanced Robotics, pp. 720–725.
[61] Costa, N., Artrit, P., and Caldwell, D. G., 2002, Soft interfaces for a humanoid robot-karate robot, John Wiley & Sons.
[62] Haswell, “MX87QD Mini ITX Motherboard” [Online]. Available: http://www.bcmcom.com/bcm_product_MX87QD.htm. [Accessed: 04-Apr-2017].
[63] Mantracourt, “Digital Load Cell Converter - DSC” [Online]. Available: http://www.mantracourt.com/products/signal-converters/digital-load-cell-converters. [Accessed: 04-Apr-2017].
[64] NXP, “PCA9544A 4-Channel Multiplexor” [Online]. Available: http://www.nxp.com/products/interfaces/ic-bus-portfolio/ic-multiplexers-switches/4-channel-i2c-bus-multiplexer-with-interrupt-logic:PCA9544A. [Accessed: 04-Apr-2017].
[65] Emart, “4 Route MOSFET Button IRF540 V4.0” [Online]. Available: http://www.emartee.com/product/42102/Arduino 4 Route MOSFET Button IRF540 V2.0. [Accessed: 04-Apr-2017].
[66] Digikey, “Honeywell HSCDANN150PG2A5” [Online]. Available: http://www.digikey.com/product-detail/en/HSCDANN150PG2A5/480-5387-5-ND/2270181. [Accessed: 04-Apr-2017].
[67] Matrix, “720 Series” [Online]. Available: http://pdf.directindustry.com/pdf/matrix-mechatronics/matrix-pneumatic-division-720-series-compact-solenoid-valve/56076-131828.html. [Accessed: 04-Apr-2017].
[68] CUI, “AMT203-V Absolute Encoder” [Online]. Available:

https://www.digikey.com/product-detail/en/cui-inc/AMT203-V/102-2050-ND/2278846. [Accessed: 04-Apr-2017].

[69] MGF, “Silent Air Compressor” [Online]. Available: http://www.mgfcompressors.com/products/silent-compressors/silent-car-lubricated-from-100-lt/p/sil-eol-50100-car/. [Accessed: 04-Apr-2017].

[70] Radionics, “AWG30-F02G1H” [Online]. Available: http://uk.rs-online.com/web/p/fr-assemblies/2550717895/. [Accessed: 04-Apr-2017].

[71] Doumit, M., Fahim, A., and Munro, M., 2009, “Analytical modeling and experimental validation of the braided pneumatic muscle,” IEEE Trans. Robot., **25**(6), pp. 1282–1291.

[72] Kothera, C. S., Jangid, M., Sirohi, J., and Wereley, N. M., 2009, “Experimental characterization and static modeling of McKibben actuators,” J. Mech. Des., **131**(9), p. 91010.